

Active topological phase transitions in high-order elastic topological insulators driven by pneumatic methods and liquid metals

Cite as: J. Appl. Phys. **133**, 104504 (2023); <https://doi.org/10.1063/5.0141556>

Submitted: 06 January 2023 • Accepted: 21 February 2023 • Published Online: 13 March 2023

 Hui-Kai Zhang,  Wei-Tong Chen,  Shi-Hao Xu, et al.



View Online



Export Citation



CrossMark



Time to get excited.
Lock-in Amplifiers – from DC to 8.5 GHz



[Find out more](#)

 Zurich
Instruments

Active topological phase transitions in high-order elastic topological insulators driven by pneumatic methods and liquid metals

Cite as: J. Appl. Phys. 133, 104504 (2023); doi: 10.1063/5.0141556

Submitted: 6 January 2023 · Accepted: 21 February 2023 ·

Published Online: 13 March 2023



View Online



Export Citation



CrossMark

Hui-Kai Zhang,¹ Wei-Tong Chen,² Shi-Hao Xu,¹ Jian Wu,² Bo Li,¹ and Xi-Qiao Feng^{1,3,a)}

AFFILIATIONS

¹ Department of Engineering Mechanics, AML, Institute of Biomechanics and Medical Engineering, Tsinghua University, Beijing 100084, China

² Department of Engineering Mechanics, AML, Institute of Solid Mechanics, Tsinghua University, Beijing 100084, China

³ Laboratory of Flexible Electronics Technology, Tsinghua University, Beijing 100084, China

^{a)}Author to whom correspondence should be addressed: fengxq@tsinghua.edu.cn

ABSTRACT

Active topological phase transitions widely occur in active matters and biological systems, such as developing embryos. Since the discovery of the intriguing bulk-boundary effects of topological insulators in Hermitian and non-Hermitian systems, various electric, optical, acoustic, and mechanical topological metamaterials with efficient energy transmission and robust defect-immunization have been designed. To date, however, it remains a challenge to precisely and fast manipulate the topological phase transitions in elastic topological insulators. In this paper, on the basis of theoretical analysis and numerical simulations, we propose an active strategy to achieve this aim through a combination of pneumatic actuation and liquid metals. The proposed method can precisely tune the connecting stiffness and vertex mass in the tight Su-Schrieffer-Heeger model. Thus, we realize the effective and fast control of topological phase transitions and elastic wave bandgap switching. We also uncover the active spinning bulk-boundary effects and higher-order topological states in the elastic topological insulators, demonstrating the high effectiveness and practicability of the proposed method. In addition, the differences between the 1D edge and 0D corner higher-order states are specified by information entropy theory. This work not only gains insights into the active manipulation of topological phase transitions but also inspires novel strategies to design active topological materials through untethered methods, e.g., magnetism or biological cells.

Published under an exclusive license by AIP Publishing. <https://doi.org/10.1063/5.0141556>

I. INTRODUCTION

The discovery of the quantum Hall effect and the quantum spin Hall effect in two-dimensional (2D) materials^{1–8} is beyond the classification of spontaneous symmetry breaking.^{8,9} Due to the intriguing bulk-boundary effect of the quantum Hall state, the electric current can pass along the 2D sample edges and, thus, avoid dissipation in the bulk.^{7–11} The edge state exhibits great robustness to the geometric defects in the material and promotes the highly efficient transmission of energy or information without backscattering.^{10,12,13} In the 2D honeycomb-net model (also referred to as “2D graphite”), Haldane^{14,15} introduced two parameters, t_1 and t_2 , to describe the electrons hopping between the nearest- and second-neighbor bonds in a lattice system. Their model does not require

an external magnetic field.¹⁴ Due to the difference of t_1 and t_2 , the time-reverse symmetry of the lattice system is broken, rendering the presence of topological (with nonzero topological invariants) and trivial states. The hopping parameters in the 2D or three-dimensional (3D) artificial microstructures can be determined by using the Hermitian model^{4,10,13,16–20} or the non-Hermitian tight Su-Schrieffer-Heeger (SSH) model.^{21–26}

With the rapid development of additive manufacturing technology, advanced materials with complex topologies can be fabricated. Thereby, several one-dimensional (1D), 2D, and 3D tight models in experiments have been proposed to achieve specified functionalities, for example, topological phase transitions^{27–35} and higher-order topological states^{17,29,36–50} in Hermitian systems, and exceptional points^{51–57} and skin effects^{21,22,25,26,58} in the

non-Hermitian system.²⁴ For different topological functional metamaterials, periodic lattice structures consisting of unit cells can be designed by varying, for example, the distances of lattice vertices,^{16,17,19,36,45,47,59,60} the symmetry breaking of vertex masses,^{61–72} the rotation of inclusions,^{40,73–79} the connecting tube diameters,^{29,38,39,41–43,49,80,81} and the stiffness of springs.^{6,82–85} Besides, the optimization of microstructured metamaterials can be performed by using inverse analysis methods, such as topology optimization^{86–91} and machine learning methods.^{92–95} To achieve fast switching control of the degeneracy points and topological phase transitions, these methods need to rebuild new structures.⁹⁶

In nature, many biological systems utilize different mechanisms to achieve their multiple functions. For instance, cytoskeleton^{97,98} can make a fast self-adapting deformation and re-organization which plays a critical role in cell metastasis.^{98,99} To protect themselves, Chameleons,¹⁰⁰ *Parachinsectsn innesi*,¹⁰¹ and *Charidotella egredia*¹⁰² can instantaneously change their colors through actively tuning the crystal morphologies in their skin cells. These intelligent active control methods of biological systems have attracted much attention in artificial functional metamaterial designs.

On the one hand, the actuation methods of light,^{103–105} magnetism,^{106–111} electricity,^{22,65,112–114} air pressure,^{82,115–128} heat,^{129–132} mechanical strain,^{133,134} and biochemistry^{135–147} are taken to drive microstructured complex deformation modes, such as tension, compression, bending, twisting, and their combinations.^{103,111} On the other hand, these active, manipulated behaviors of deformations and motions in structures may also affect their topological properties in energy or information transmissions. For instance, spinning gyroscopes,^{148–151} rotors,^{152,153} Floquet mechanisms,¹⁵⁴ fluid chambers,^{65,155} and movable components¹⁵⁶ are used to tune the effective microstructured masses, which determine their topological or trivial states. Besides, the dielectric elastic composite films^{59,157–159} and piezoelectric beams^{160,161} can be electrically actuated to achieve the topological phase transitions in elastic,⁹⁶ acoustic, and photonic insulators. Up to now, however, a facile and highly effective strategy for the design of active, intelligent topological metamaterial remains an open challenge.^{162–165}

In this paper, inspired by Chameleons, starfish pipes,¹⁶⁶ and cell communication,¹⁶⁷ we propose a novel pneumatic actuation method that can actively manipulate the deformations, connected chamber stiffnesses, and vertex masses of the 1D and 2D elastic SSH lattice models. This paper is organized as follows. In Sec. II, the proposed active pneumatic actuation method is described. The relations of connected chamber stiffness and vertex mass (liquid metal) with respect to the active air pressures are uncovered. In Sec. III, on the basis of numerical and theoretical analysis of composite microstructures, the proposed active method successfully manipulates the switching of degeneracy points in the dispersion spectrums. Then, the active topological phase transitions with respect to the driven air pressures in the microstructures are analyzed in Sec. IV. In Sec. V, the active bulk-boundary effects, including the quantum spin or valley Hall effects (QSHE and QVHE), are precisely manipulated through the proposed pneumatic strategy. Furthermore, the complex active interfaces are automatically constructed by the proposed method and used to obtain active higher-order topological states in Sec. VI.

Besides, the information entropy theory is also employed to distinguish the lower and higher states.

II. ACTIVE PNEUMATIC ACTUATION MODEL

Chameleons can fast and actively tune their skin color, when they are in a dangerous environment [Fig. 1(a)]. In an excited state, the osmotic pressure in the skin cells increases instantaneously, which increases the cell volume. Therefore, the distance of Guanine crystals in the skin cells becomes larger, thus resulting in a blue shift in the reflectivity of s-iridophores [Fig. 1(a)]. Inspired by this active mechanism, we propose a pneumatic control strategy to actively manipulate the 1D composite structure composed of the soft air chambers (blue color) and liquid metals (red color) [Figs. 1(b) and 9(a)].

Based on the tight SSH model [Fig. 1(b)], we define a composite unit cell consisting of two metallic masses and two air chambers connected together. The left (yellow box) and right (green box) chambers have the intracell and intercell connected stiffness $k_1(P_K)$ and $k_2(P_K)$, respectively. Besides, the left and right liquid metals have varying masses $m_1(P_M)$ and $m_2(P_M)$. P_K and P_M are the active air pressures.

A. Active change of connected stiffnesses

First, in each unit cell, the connected intracell air chamber can actively deform under the actuation of suction ($P_K < 0$) or inflation ($P_K > 0$) [Fig. 1(c)], while the intercell air chamber cannot. Therefore, the intracell chamber has a shrinking or expanding deformation mode with the active air pressure $P_K < 0$ or $P_K > 0$, which can be calculated by the nonlinear finite element method (Appendix B).

In this model, we take the characteristic size of unit cells as $a = 40$ mm, which was determined according to our fabrication method. Thus, the intercell chamber may undergo expanding or shrinking deformations caused by the shift of the intracell chamber [Fig. 1(c)]. For instance, the displacement fields of the second mass are shown in Fig. 1(e). Once the active actuation has been removed, all deformation modes [Fig. 1(c)] of the unit cell may return to its initial state with $P_K = 0$.

The deformation of the unit cell is calculated through numerical simulations, and then the deformed geometries of the air chambers are exported for the uniaxial compression test. For simplicity, we ignore the effects of stress on the chamber stiffness. In Fig. 1(c), the bottom regions of the deformed chambers are fixed, and we apply a y -direction displacement \mathbf{u} on the top surfaces of the chambers. Through finite element calculations, the compression stiffnesses of the intercell and intracell chambers under prescribed air pressures P_K can be obtained.

In Fig. 1(f), we uncover the nonlinear relations of the varying stiffness k_1 (intracell) and k_2 (intercell) with respect to P_K . At the initial state, the stiffness satisfies $k_1(P_K = 0) = k_2(P_K = 0)$. As the actuation has $P_K < 0$, the intracell stiffnesses $k_1(P_K)$ (green points) are smaller than the intercell stiffness $k_2(P_K)$ (red points). Once the pneumatic actuation P_K is positive, the intracell stiffness $k_1(P_K)$ becomes larger than the intercell stiffness $k_2(P_K)$. The reason is that the chamber walls in the negative air pressures or compression states are easier to buckle, which results in a low stiffness. Further,

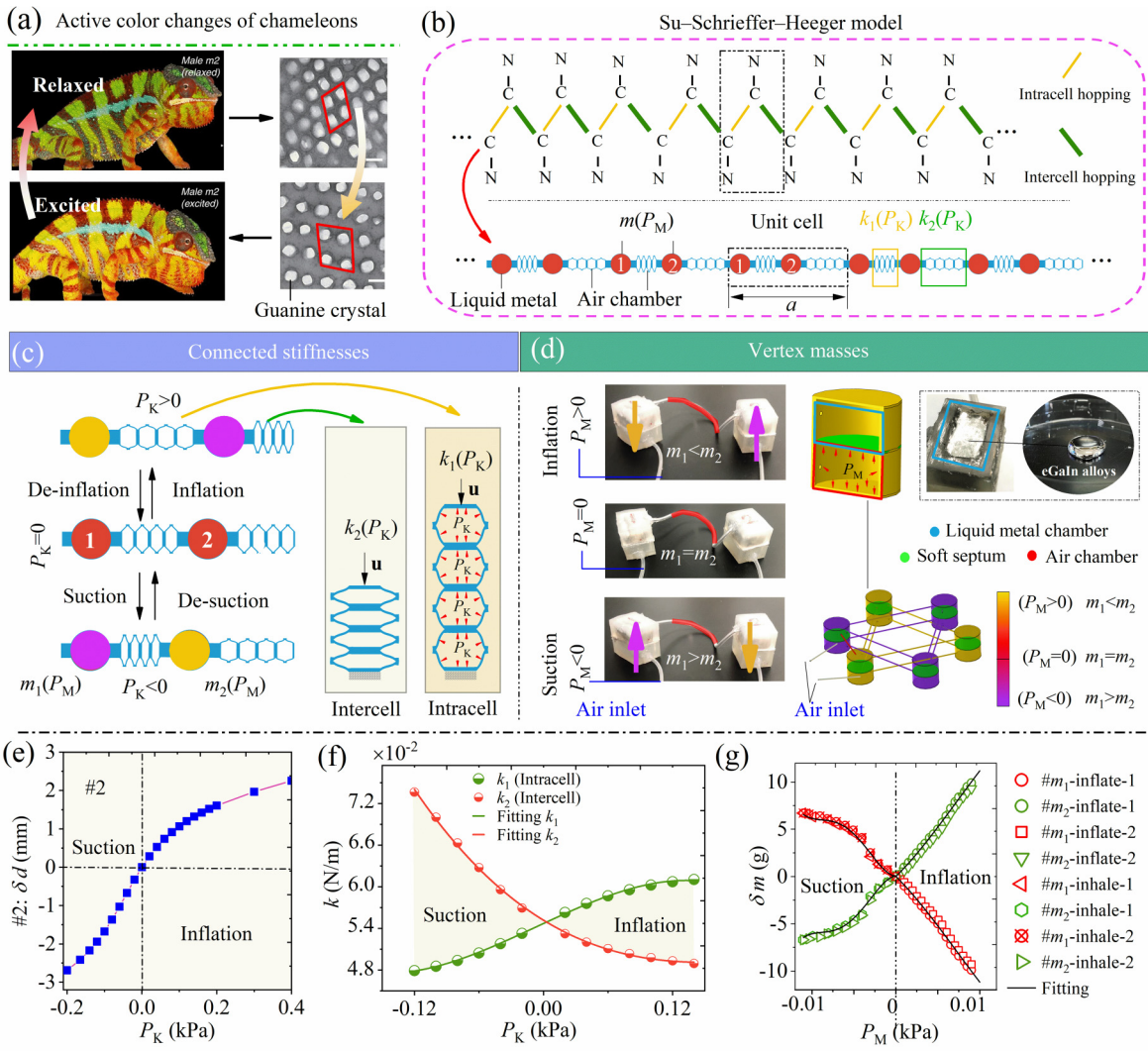


FIG. 1. Active exchange of the connected air chamber stiffness and vertex mass. (a) Actively and fast color tuning mechanism of chameleons.¹⁰⁰ Reproduced with permission from Teyssié *et al.*, Nat. Commun. **6**, 1–7 (2015). Copyright 2015, Author(s) under a Creative Commons Attribution (CC BY) license. In the excited state, the distance of the guanine crystals becomes smaller compared to the patterns in the relaxed state generated by the bio-chemo-mechanical control. (b) The tight Su-Schrieffer-Heeger (SSH) model composed of “C–N” bonds. The yellow (intracellular) and green (intercellular) chemical bonds have different strengths. In the bottom of (b), a 1D composite active structure is constructed, in which the red masses and blue structures are the liquid metal and air chambers. (c) The unit cell of the active elastic SSH model, in which the connected air chambers’ stiffnesses can be manipulated by suction or inflation. (d) The active mass exchange can be achieved through the combination of air and liquid metal chambers (eGaN alloys), which also allows us to measure the mass exchange. (e) Displacements of specimen #2 vs the active air pressures. (f) The relations of intracellular and intercellular air chamber stiffnesses with respect to the active air pressure P_K. (g) The vertex masses vs the active air pressure P_M.

this precise relation of $k_i - P_K$ ($i = 1, 2$) [Fig. 1(f) and Table I] is

$$\begin{aligned} k_1(P_K) &= 0.055 + 0.073P_K - 0.032P_K^2 - 1.415P_K^3, \quad P_K \\ &\in [-0.25, 0.2] \text{ kPa}, \end{aligned} \quad (1)$$

$$\begin{aligned} k_2(P_K) &= 0.055 - 0.096P_K + 0.458P_K^2 - 0.383P_K^3, \quad P_K \\ &\in [-0.25, 0.2] \text{ kPa}. \end{aligned} \quad (2)$$

A larger deformation of the intracellular and the intercellular chambers may stop the numerical calculations. The active air pressures P_K are suggested in the interval $[-0.25, 0.2]$ kPa.

B. Active change of masses

Starfish can fast store and discharge water due to its unique pipe systems.¹⁶⁶ Besides, a tuning nanotube (TNT) between two cells makes it possible to achieve cell communication over a long

TABLE I. Stiffness of the intracell and intercell chambers vs P_K .

P_K (kPa)	Suction								
	-0.2	-0.165	-0.14	-0.12	-0.10	-0.08	-0.06	-0.04	-0.02
k_1 (N/m)	0.047	0.047	0.048	0.048	0.049	0.049	0.051	0.052	0.053
K_2 (N/m)	0.085	0.081	0.077	0.074	0.0700	0.066	0.063	0.060	0.057
P_K (kPa)	Inflation								
	0.02	0.04	0.06	0.08	0.1	0.12	0.14	0.16	0.18
k_1 (N/m)	0.056	0.058	0.059	0.060	0.060	0.061	0.061	0.061	0.061
K_2 (N/m)	0.053	0.052	0.051	0.050	0.050	0.049	0.049	0.048	0.048

distance.¹⁶⁴ The macromolecular organelles and Ca^+ ions can transport from one cell to another through the TNT, which are important physiological phenomena in cancer cell metastasis.

Inspired by these active mechanisms, the mass exchange of metallic particles #1 and #2 is possible. To achieve this goal, we construct two structures connected by a soft tube [red color in Fig. 1(d), and Figs. 9(b) and 9(c)]. Each structure has two subspaces separated by a thin septum [green color in Fig. 1(d)]. The top (blue color) and bottom (red color) spaces are the liquid metal and air chambers. At the initial state, the top subspace of each structure is infilled with the same liquid metal eGaIn

alloys,^{168,169} and the connecting tube is also encapsulated with the liquid metal.

Further, the left air chamber is actuated with $P_M > 0$, and it has an expanding deformation [Fig. 1(d)]. The deformation may push the liquid metal in the top liquid chamber of the left structure into the top liquid chamber of the right structure, which eventually has $m_1(P_M) < m_2(P_M)$. When the P_M is negative, the left-bottom air chamber has a shrinking deformation, which finally results in $m_1(P_M) > m_2(P_M)$. These actuations are fast and reversible. Figure 1(g) gives the precise relation of δm and P_M by performing twice experimental tests (Tables II and III), and they are

$$\delta m_1(P_M) = \begin{cases} 0.0022P_M^3 - 0.0474P_M^2 - 0.864P_M + 0.0029, & P_M(\text{kPa}) \geq 0, \\ 0.0026P_M^4 + 0.0616P_M^3 + 0.4132P_M^2 - 0.0384P_M P + 0.0392, & P_M(\text{kPa}) \leq 0, \end{cases} \quad (3)$$

$$\delta m_2(P_M) = \begin{cases} -0.0022P_M^3 + 0.0474P_M^2 + 0.864P_M - 0.0029, & P_M(\text{kPa}) \geq 0, \\ -0.0026P_M^4 - 0.0616P_M^3 - 0.4132P_M^2 + 0.0384P_M P - 0.0392. & P_M(\text{kPa}) \leq 0, \end{cases} \quad (4)$$

where $P_M \in [-0.01, 0.01]$ kPa, and δm_i is the value of mass change. This dimeric system can be extended to the complex honeycomb lattice [Fig. 1(d)] by adding some connecting tubes in the corresponding chambers. In the numerical eigenanalysis, the varying material density of the liquid metal is written as

$$\rho_{L,i}(P_M) = \rho_0 + \frac{\delta m_i(P_M)}{V_0 \eta}, \quad (5)$$

where $\rho_0 = 7.4 \times 10^{-3}$ g mm⁻³ is the density of the nickel neodymium magnet,³³ which is close to the density of liquid metal eGaIn alloy 6×10^{-3} g mm⁻³. $V_0 = \pi r_0^2 t$ is the constant volume with $r_0 = 3.4$ mm and $t = 1$ mm [Fig. 9(a)]. Therefore, the balancing mass is $m_0 = \rho_0 V_0 = 0.269$ g with $P_M = 0$ in all calculation models. To obtain a suitable change of density, we suggest that the penalty factor η is set at 50 in the simulations, and all varying densities of liquid metal are listed in Table IV. Besides, the elastic modulus and Poisson's ratio are assumed to be 41 GPa and 0.28, respectively.

In the pneumatic strategy, P_K and P_M have different functionalities for actively tuning the connected stiffness and vertex mass, respectively. In Secs. III A–III C, we extend these relations [Figs. 1(f) and 1(g)] to research the active topological effects in 1D and 2D systems.

III. ACTIVE SWITCHING OF DIRAC POINTS

In this section, we uncover the effects of the active stiffnesses and masses on the bandgaps by extending the 1D SSH model [Fig. 1(c)] to the 2D C_4 , C_6 , and C_3 microstructures. Based on the periodic Bloch theory, we calculate the dispersion curves of all 1D and 2D unit cells under different pneumatic pressures (P_K or P_M) through numerical simulations and theoretical analysis.

A. Deformations of 2D models

In this subsection, we design three types of 2D unit cells [Figs. 2(a)–2(c)] through the combination of 1D SSH models [Fig. 1(c)]. In Fig. 2(a), the square unit cell with C_4 symmetry

TABLE II. Mass changes of the liquid metallic chambers with $P_M > 0$.

$P_M (\times 10^{-3})$	First test, pressure (kPa), mass (g)				Second test, pressure (kPa), mass (g)				
	m_1	m_2	δm_2	δm_1	$P_M (\times 10^{-3})$	m_1	m_2	δm_2	δm_1
0	20.4	18.8	0.0	0.0	0.00	18.8	20.4	0.0	0.0
0.43	20.2	19.0	0.2	-0.2	0.53	18.5	20.7	0.3	-0.3
1.00	19.4	19.8	1.0	-1.0	1.00	18.2	21.0	0.6	-0.6
1.54	18.9	20.3	1.5	-1.5	1.49	17.8	21.4	1.0	-1.0
2.03	18.4	20.8	2.0	-2.0	2.00	17.3	21.9	1.5	-1.5
2.49	17.9	21.3	2.5	-2.5	2.51	16.7	22.5	2.1	-2.1
3.06	17.3	21.9	3.1	-3.1	3.05	16.2	23.0	2.6	-2.6
3.50	16.9	22.3	3.5	-3.5	3.55	15.6	23.6	3.2	-3.2
4.02	16.3	22.9	4.1	-4.1	4.08	15.2	24.0	3.6	-3.6
4.50	15.9	23.3	4.5	-4.5	4.44	14.8	24.4	4.0	-4.0
5.00	15.4	23.8	5.0	-5.0	5.08	14.2	25.0	4.6	-4.6
5.52	14.7	24.5	5.7	-5.7	5.51	13.7	25.5	5.1	-5.1
6.00	14	25.2	6.4	-6.4	6.05	12.9	26.3	5.9	-5.9
6.55	13.2	26	7.2	-7.2	6.53	12.2	27.0	6.6	-6.6
7.07	12.5	26.7	7.9	-7.9	7.05	11.5	27.7	7.3	-7.3
7.50	12.0	27.2	8.4	-8.4	7.49	11	28.2	7.8	-7.8
8.20	11.4	27.8	9.0	-9.0	8.02	10.4	28.8	8.4	-8.4
8.50	10.9	28.3	9.5	-9.5	8.51	9.9	29.3	8.9	-8.9
9.00	10.5	28.7	9.9	-9.9	9.02	9.5	29.7	9.3	-9.3

contains the same four metallic masses and twelve air chambers, and its crystal constant is a [Fig. 10(a) in Appendix B]. The internal four air chambers are the active components that can be actuated by the pneumatic pressures P_K , which results in the shrinking and expanding deformations in the C_4 unit cell [the processes I–IV in Fig. 2]. Here, we assume that the deformed air chambers in the C_4 unit cell have varying intracell and intercell stiffnesses as expressed in Eqs. (1) and (2), respectively. Similarly, we also use the 1D model to construct a 2D unit cell with C_6 symmetry [Fig. 2(b)], which has the six same metallic masses and twelve air chambers [Fig. 10(d) in Appendix B]. The crystal constant of the

unit cell is $l = 34.64$ mm. The internal six air chambers can be actuated by the pneumatic pressures P_K , which also promotes the shrinking and expanding deformations of the unit cell [Fig. 2(b)]. Besides, the intracell and intercell stiffnesses also satisfy Eqs. (1) and (2).

The third unit cell is given in Fig. 2(c), and it has five air chambers and two variable metallic masses with a crystal constant $s = l$. For this unit cell, we assume that all air chambers are inactive, and the two metallic parts can exchange their masses through the proposed air–liquid chamber model as shown in Fig. 1(d). The entire superstructure [Fig. 10(g) in Appendix B] can be obtained

TABLE III. Mass changes of the liquid metallic chambers with $P_M < 0$.

$P_M (\times 10^{-3})$	First test, pressure (kPa), mass (g)				Second test, pressure (kPa), mass (g)				
	m_1	m_2	δm_2	δm_1	$P_M (\times 10^{-3})$	m_1	m_2	δm_2	δm_1
0.00	19.4	19.8	0.0	0.0	0.0	18.7	20.5	0.0	0.0
-1.00	20.0	19.2	-0.6	0.6	-1.0	19.4	19.8	-0.7	0.7
-2.08	20.7	18.5	-1.3	1.3	-2.1	20	19.2	-1.3	1.3
-3.06	21.5	17.7	-2.1	2.1	-3.0	21.2	18	-2.5	2.5
-4.02	23.4	15.8	-4.0	4.0	-4.0	22.8	16.4	-4.1	4.1
-5.03	24.0	15.2	-4.6	4.6	-5.1	23.6	15.6	-4.9	4.9
-6.02	24.6	14.6	-5.2	5.2	-6.1	24.1	15.1	-5.4	5.4
-7.02	24.9	14.3	-5.5	5.5	-7.1	24.5	14.7	-5.8	5.8
-8.04	25.4	13.8	-6.0	6.0	-8.2	24.8	14.4	-6.1	6.1
-9.90	25.7	13.5	-6.3	6.3	-9.1	25.1	14.1	-6.4	6.4
-10.60	26.0	13.2	-6.6	6.6	-10.3	25.3	13.9	-6.6	6.6
-11.10	26.1	13.1	-6.7	6.7	-11.0	25.4	13.8	-6.7	6.7

TABLE IV. Effective densities (10^{-3} g mm $^{-3}$) vs P_M in the active model.

P_M (kPa) $\times 10^{-3}$	0	1	2	3	4	5	6	7	8	9	10
# ρ_1	7.40	6.89	5.77	5.77	5.16	4.52	3.87	3.21	2.54	1.89	1.24
# ρ_2	7.40	7.90	9.03	9.03	9.64	10.30	10.9	11.6	12.3	12.9	13.6
P_M (kPa) $\times 10^{-3}$	-1	-2	-3	-4	-5	-6	-7	-8	-9	-10	-11
# ρ_1	7.62	8.10	8.71	9.32	9.85	10.25	10.5	10.63	10.69	10.76	10.98
# ρ_2	7.18	6.70	6.09	5.48	4.95	4.55	4.30	4.17	4.11	4.03	3.82

by making an array of this unit cell, and the active mass exchange is possible to take place in the superstructure by adding some connecting soft tubes [Fig. 1(d)]. Under the I–IV actuators by P_M , the weight changes of the metallic masses in the unit cell [Fig. 2(c)] satisfy Eqs. (3) and (4). Besides, the mass symmetry of the superstructure [Fig. 7(g)] changes from C_6 to C_3 .^{61,63,69,72,83,158,170}

All deformations and mass changes in the 1D and 2D unit cells can be precisely manipulated by the proposed pneumatic strategy, which paves a way for the following investigation of the physical functionalities of bandgaps.

B. Calculations of bandgaps

According to the results of the deformations and mass changes obtained in Sec. III A, we take the Bloch theory (Appendix B) to study the changes of elastic wave bandgaps in different 1D and 2D unit cells under varying active pneumatic pressures P_K or P_M .

First, we take the 1D unit cell as an example. Three deformation modes of the unit cell are shown in Fig. 1(c) with the active pneumatic pressures $P_K = -0.140$, 0, and 0.20 kPa, and P_M is kept zero in these processes. Once the calculations of deformations are completed, we export these deformed geometries for the following eigenanalysis. To ensure the 1D unit cell to have the eigenmodes in the x -direction, we fix all the y -direction freedoms in the eigenanalysis. Figure 2(d) shows three types of dispersion curves highlighted by green, red, and blue colors with the corresponding P_K . At the initial state $P_K = 0$, the intracell and intercell stiffnesses satisfy $k_1(P_K) = k_2(P_K)$, which results in a degeneracy at $k_x = \pm\pi/|a|$ and a closed bandgap in the red dispersion curves. Once the 1D unit cell deviates away from its equilibrium state with $P_K \neq 0$, the broken symmetry of the hopping stiffnesses $k_1(P_K)$ and $k_2(P_K)$ may induce the degenerated Dirac point (DP) to open instantaneously [green and blue colors in Fig. 2(d)].

Similarly, the dispersion curves of the 2D unit cells with C_4 ($P_K = -0.01$ and 0.20 kPa) and C_6 ($P_K = -0.1$ and 0.16 kPa) symmetries are also calculated in the corresponding Brillouin zones [Figs. 10(b) and 10(e)]. There is no doubt that the degeneracy points occur at X and Γ [Figs. 2(e) and 2(g)] in their initial states with $P_K = 0$. The double-degeneracy DP in the C_6 unit cell is caused by the higher C_6 symmetry, and this feature promotes the fold of the first irreducible Brillouin zones [Fig. 10(e)].^{6,36,59,160} This double degeneracy is widely observed in topological insulators that have QSHE.^{7,8} Once the active actuators start to work, the opening bandgaps can be obtained, and this active process from $P_K = 0$ to $P_K \neq 0$ takes a short time [Figs. 2(e) and 2(g)].

In the third example [Fig. 2(c)], the intracell and intercell stiffnesses are set as $k_1 = k_2$ ($P_K \equiv 0$). In Fig. 2(i), at the initial states $P_M = 0$, two masses in the unit cell are $m_1 = m_2$ and the unit cell has a higher C_6 symmetry. Two degeneracy points appear at the K and K' in the Brillouin zone [Fig. 10(h)], and they form two valleys and peaks. This feature plays a key role in the QVHE.^{5,68,69,83,84,171} If the actuation P_M begins to work, such as $P_M = -0.01$ and 0.01 kPa, these closed degeneracy points can open immediately [Fig. 2(i)].

C. Theoretical analysis

Now, we further construct an active spring-mass model to calculate the bandgaps under different pneumatic pressures. The active Lagrangian function^{6,83,84,172,173} is given as

$$L(P_K, P_M) = \frac{1}{2} m_i(P_M) \left(\dot{\mathbf{u}}_i^{(p)} \right)^2 - \frac{1}{2} \sum_{i,j,i \neq j} k_{i(p,q),j(t,s)}(P_K) \left[(\mathbf{u}_{i(p,q)} - \mathbf{u}_{j(t,s)}) \cdot \mathbf{e}_{i(p,q)-j(t,s)} \right]^2, \quad (6)$$

where \mathbf{u} and \mathbf{e} are the vectors of the mass displacements and the directions of the connecting springs in the x – y coordinate [Figs. 10(c), 10(f), and 10(i)]. $\dot{\mathbf{u}} = d\mathbf{u}/dt$ is the velocity of the vertex mass. (p, q) is the index of the unit cell for the 2D lattices. The first term provides the active kinematic contribution from $m_i(P_M)$, and it is

$$m_i(P_M) = m_0 + \delta m_i(P_M), \quad (7)$$

where $m_0 = \rho_0 V_0$, and the second term mainly represents the active potential energy raised from the connected stiffnesses $k_{i,j}(P_K)$. i and j represent the number of vertex mass.

Inserting Eqs. (1)–(4) into Eq. (6) leads to the following eigen-equation (Appendix B):

$$[\mathbf{H}_{n \times n}(P_K) + \omega^2 \mathbf{M}_{n \times n}(P_M)] \bar{\mathbf{u}}_{n \times 1} = \mathbf{0}, \quad (8)$$

where $\mathbf{H}(P_K)$ and $\mathbf{M}(P_M)$ are the active Hamilton and mass matrices, ω is the angular frequency, and n is the dimension of the mass freedoms in the corresponding unit cells, for example, $n = 4$ for the 1D case and $n = 12$ for the C_6 unit cell.

For each case, the first irreducible Brillouin zone [Fig. 10] and the entire Brillouin zone are taken in the theoretical analysis. In Figs. 2(f), 2(h), and 2(j), for a clear presentation of the results, we just calculate two air pressures in each case, and these theoretical

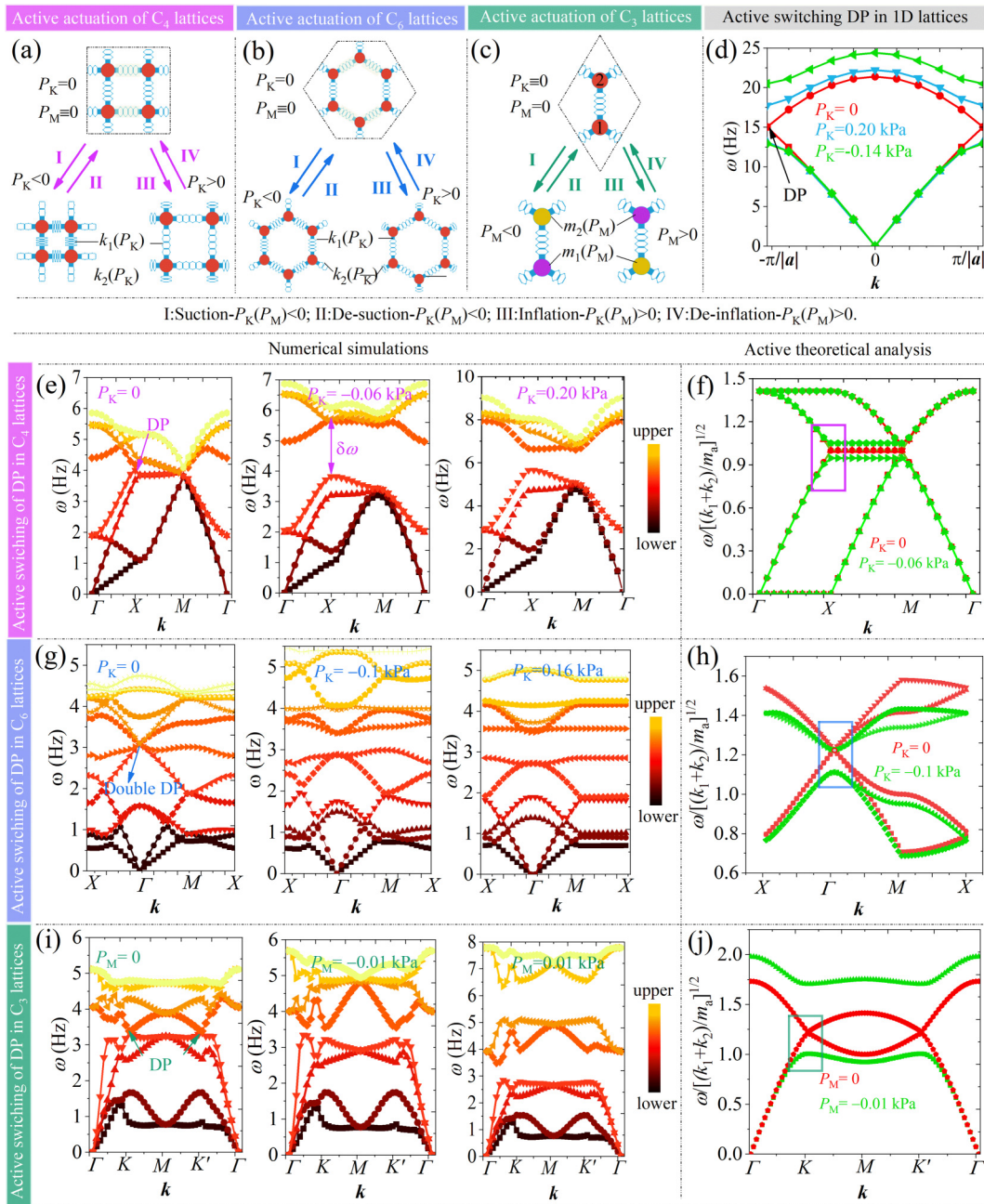


FIG. 2. Active bandgap switching of the dispersion curves in 1D and 2D lattices. (a) A C_4 unit cell is constructed by the combination of the 1D unit cell [Fig. 1(c)], and it has shrinking and expanding deformations under the actuations P_K of suction and inflation. (b) A C_6 unit cell is constructed by the combination of the 1D unit cell [Fig. 1(c)], and it also has a shrinking and expanding deformation under the actuations P_K of suction and inflation. (c) A C_3 unit cell is constructed by the combination of the 1D unit cell [Figs. 1(c) and 1(d)], and its mass symmetry is broken under the actuations P_M . (d) The active switching of the Dirac points (DPs) in the 1D unit cell is manipulated by the pneumatic methods. (e) The dispersion curves of the C_4 lattice are calculated under varying air pressures P_K , and the opening and closing of the degeneracy DP are also actively manipulated by P_K . $\delta\omega$ is the opening width of the DP. The color bar denotes the frequencies from lower (black) to upper (yellow) orders. (f) The dispersion curves are calculated based on the active spring-mass model. (g) and (h) The dispersion curves of the C_6 lattice. The double-degeneracy DPs are the feature of the quantum spin Hall effect. In addition, we ignore some curves in (i) for a clear elucidation. (i) and (j) The dispersion curves of the C_3 lattice. The two valley-peak shapes at the degeneracy points denote that the unit cell has the quantum valley Hall effect with $m_1 \neq m_2$ ($P_M \neq 0, P_K = 0$). All masses shown in (d)–(h) have the same value m_0 , and the active pneumatic pressure is $P_M = 0$ ($P_K \neq 0$). m_a is an average mass, taken as $(m_1 + m_2)/2$.

TABLE V. Degeneracy points vs the active actuation $P_K(C_4)$.

P_K (kPa)	-0.14	-0.12	-0.095	-0.08	-0.06	-0.04	-0.02	0	0.02	0.04
#1(Hz)	3.22	3.27	3.35	3.41	3.50	3.61	3.73	3.84	3.72	3.63
#2(Hz)	3.83	3.87	3.92	3.97	4.04	4.13	4.00	3.85	3.97	4.08
#3(Hz)	5.64	5.31	4.91	4.69	4.42	4.19	4.23	4.33	4.22	4.13
#4(Hz)	5.71	5.61	5.35	5.14	4.88	4.66	4.48	4.34	4.44	4.54
P_K (kPa)	0.06	0.08	0.10	0.12	0.14	0.16	0.18	0.20	0.22	
#1(Hz)	4.18	4.27	4.35	4.42	4.48	4.53	4.57	4.60	4.63	
#2(Hz)	4.64	4.72	4.80	4.86	4.92	4.96	5.00	5.03	5.06	
#3(Hz)	3.54	3.49	3.44	3.39	3.36	3.33	3.30	3.28	3.25	
#4(Hz)	4.06	4.01	3.96	3.92	3.89	3.86	3.84	3.82	3.80	

conclusions [Figs. 2(f), 2(h), 2(g), and 11] are consistent with numerical results for different unit cells.

Taken together, we have successfully extended the 1D SSH model to construct three types of 2D unit cells. The proposed pneumatic strategy can fast and precisely manipulate the switching bandgaps of all 1D and 2D unit cells through numerical calculations and active theoretical analysis.

IV. ACTIVE TOPOLOGICAL PHASE TRANSITION

The active switching of the degeneracy DPs can be fast manipulated by the negative or positive pneumatic pressures, as demonstrated in Sec. III. In this section, we show the precise control of the opening widths of the DPs under different air pressures, because this opening width $\delta\omega$ determines the bandgaps. Besides, the relations between the active topological effects and pneumatic pressures will be established.

For each type of the 1D and 2D unit cells defined above, the active pneumatic pressures gradually change in the interval $[-0.14, 0.20]$ kPa for the 1D unit cell, $[-0.14, 0.22]$ kPa for the unit cell with C_4 symmetry, $[-0.10, 0.16]$ kPa for the unit cell with C_6 symmetry, and $[-0.01, 0.01]$ kPa for the C_3 symmetry. For a given pneumatic pressure, the eigenanalysis is calculated at the corresponding degeneracy point in the first irreducible zone (Tables V–VII). Figures 3(a), 3(c), 3(e), and 3(f) show all shifts of the degeneracy point with respect to the pneumatic pressures. The opening widths $\delta\omega$ of the DP gradually increase with the air pressure amplitudes, which are consistent with the theoretical results [Figs. 4(a)–4(d)].

In our numerical simulations, we find that the eigenmodes under $P_K < 0$ and $P_K > 0$ have different topological phenotypes. For example, in Fig. 3(a), the two frequency points at $P_K = -0.12$ kPa are marked with red and blue colors [Fig. 3(a)]. The red color denotes the higher frequency and the blue point is the lower frequency. The red point has a shrinking eigenmode, in which the distance of the two masses reduces [red arrows in Fig. 3(a)]. The blue point has an expanding eigenmode, and the two masses are away from each other [blue arrows in Fig. 3(a)]. As the air pressure becomes positive, such as $P_K = 0.20$ kPa, the shrinking and expanding eigenmodes belong to the lower (red) and higher (blue) frequencies. This change denotes the eigenmodes of the DPs have a topological phase transition with respect to the active pneumatic pressures P_K .

Further, a topological invariant winding number W in the 1D SSH model is here used to describe this process of the active topological phase transition, and the unit cell is trivial or topological with $W=0$ or $W=1$, respectively. This topological invariant reads

$$W = \frac{1}{2\pi} \int_{BZ} \left[\tilde{\mathbf{d}}(k_x, P_K) \times \frac{d}{dk_x} \tilde{\mathbf{d}}(k_x, P_K) \right] dk_x \\ = \frac{1}{2\pi} \int_{BZ} \left(\frac{d_x \partial_k d_y - d_y \partial_k d_x}{|\mathbf{d}|^2} \right) dk_x, \quad (9)$$

where $\tilde{\mathbf{d}} = \mathbf{d}/|\mathbf{d}|$. $\mathbf{d} = (d_0, d_x, d_y)$ is the vector that denotes the coefficients of Pauli matrices, and its components satisfy the following relation:

$$\hat{\mathbf{H}}_{2\times 2}(P_K) = d_0 \boldsymbol{\sigma}_0 + d_x \boldsymbol{\sigma}_x + d_y \boldsymbol{\sigma}_y, \quad (10)$$

where $\hat{\mathbf{H}}_{2\times 2}(P_K)$ is an active Hamilton matrix (Appendix B), $\boldsymbol{\sigma}_0$, $\boldsymbol{\sigma}_x$, and $\boldsymbol{\sigma}_y$ are the Pauli matrices

$$\boldsymbol{\sigma}_0 = \begin{bmatrix} 1 & 0 \\ 0 & 1 \end{bmatrix}, \quad \boldsymbol{\sigma}_x = \begin{bmatrix} 0 & 1 \\ 1 & 0 \end{bmatrix}, \quad \boldsymbol{\sigma}_y = \begin{bmatrix} 0 & -i \\ i & 0 \end{bmatrix}. \quad (11)$$

The Pauli coefficients are

$$d_0 = k_1(P_K) + k_2(P_K), \quad (12)$$

TABLE VI. Double-degeneracy points vs the active actuation $P_K(C_6)$.

P_K (kPa)	-0.1	-0.08	-0.06	-0.04	-0.02	0.00
#1(Hz)	2.88	2.86	2.94	2.98	3.00	3.00
#2(Hz)	2.88	2.90	2.94	2.98	3.00	3.00
#3(Hz)	3.40	3.32	3.32	3.25	3.17	3.00
#4(Hz)	3.40	3.37	3.32	3.25	3.17	3.00
P_K (kPa)	0.02	0.04	0.06	0.08	0.10	0.12
#1(Hz)	3.00	2.95	2.89	2.84	2.81	2.77
#2(Hz)	3.00	2.95	2.88	2.84	2.80	2.77
#3(Hz)	3.16	3.22	3.29	3.35	3.40	3.45
#4(Hz)	3.6	3.23	3.29	3.35	3.41	3.46
P_K (kPa)	0.14	0.16				
#1(Hz)						
#2(Hz)						
#3(Hz)						
#4(Hz)						

TABLE VII. Degeneracy points vs the active actuation $P_M(C_3)$.

$P_M \times 10^{-3}$ (kPa)	-11	-10	-9	-8	-7	-6	-5	-4	-3	-2	-1
#1	3.218	3.22	3.22	3.22	3.22	3.22	3.22	3.23	3.25	3.28	3.32
#2	3.556	3.54	3.53	3.53	3.52	3.50	3.49	3.48	3.46	3.43	3.40
$P_M \times 10^{-3}$ (kPa)	0	1	2	3	4	5	6	7	8	9	10
#1	3.34	3.40	3.47	3.56	3.66	3.77	3.87	3.94	3.98	3.98	3.96
#2	3.38	3.34	3.29	3.22	3.16	3.09	3.02	2.96	2.89	2.83	2.78

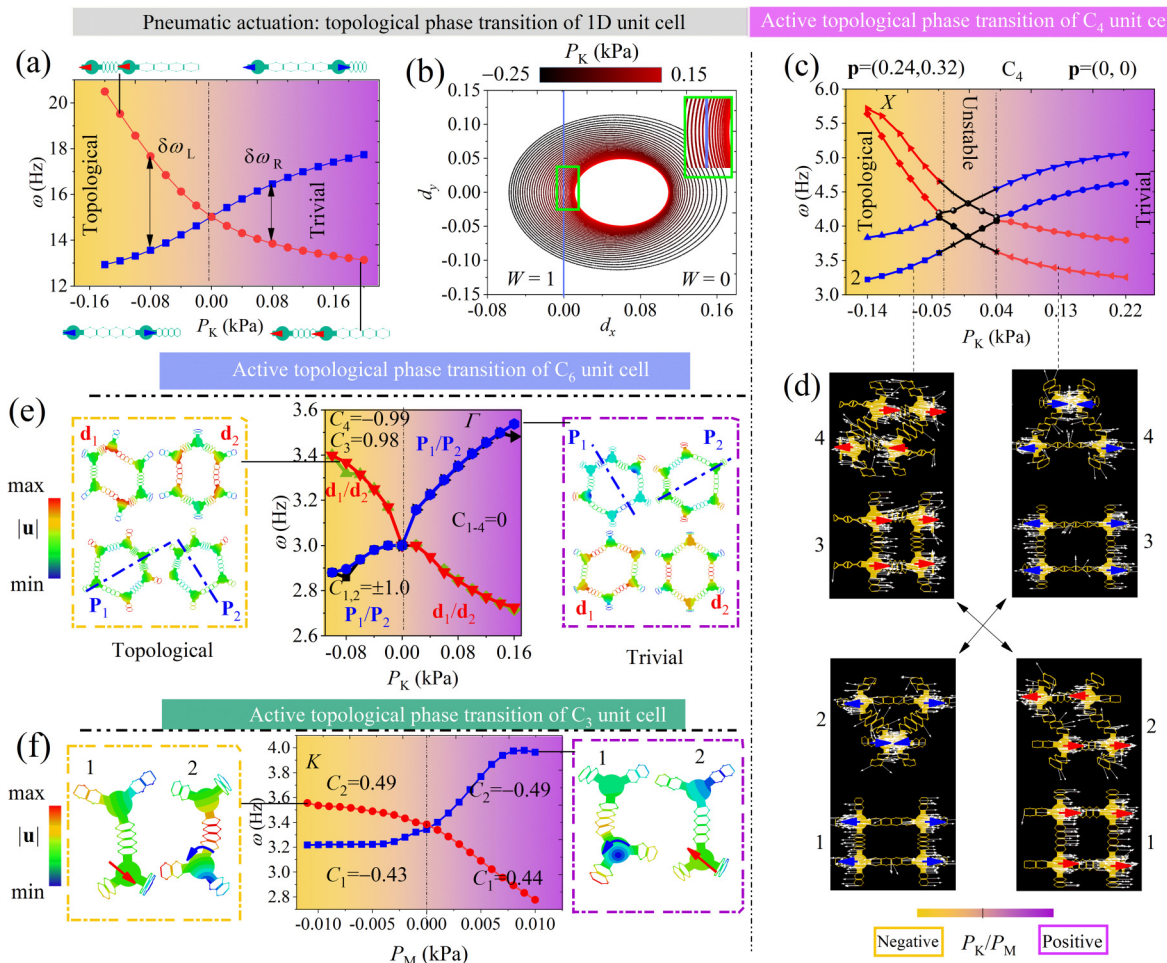


FIG. 3. Active topological phase transitions. (a) The eigenmodes of the lower (blue) and higher (red) frequency points at $P_K = -0.12$ kPa show expanding (blue arrows) and shrinking deformations (red arrows), and they occur at the higher (blue) and lower (red) frequency points with $P_K = 0.20$ kPa. $\delta\omega_L$ and $\delta\omega_R$ are the opening widths of the DPs located at the left and right sides of $P_K = 0$. (b) Topological invariant winding number W changes with the active pneumatic pressures. $W = 1$, $P_K < 0$ and $W = 0$, $P_K > 0$ denote that the unit cell is topological and trivial, respectively. (c) and (d) The active topological phase transition of the quadrupole unit cell with C_4 symmetry. Bulk polarizations are $\mathbf{P} = (0.24, 0.32)$ and $\mathbf{P} = (0, 0)$ with $P_K < 0$ (e.g., $P_K = -0.07$ kPa, topological) and $P_K > 0$ (e.g., $P_K = -0.08$ kPa, trivial), respectively. At $P_K = -0.08$ and 0.12 kPa, the corresponding eigenmodes have a distinct change. (e) The active topological phase transition of the unit cell with C_6 symmetry. At $P_K = -0.08$ and 0.16 kPa, the \mathbf{P} (polar symmetry) and \mathbf{d} (centrosymmetry) eigenmodes are different. The topological invariants, Chern numbers are $C_1 = 1.0$, $C_2 = -1.0$, $C_3 = 0.98$, and $C_4 = -0.99$ with $P_K < 0$ (e.g., $P_K = -0.05$ kPa) and $C_{1-4} = 0$ with $P_K > 0$ (e.g., $P_K = -0.05$ kPa), respectively. (f) The active topological phase transition of the quadrupole unit cell with C_3 symmetry. Under the actuation of P_M , the Chern number changes from $C_1 = -0.43$ and $C_2 = 0.49$ with $P_M < 0$ (e.g., $P_M = 0.8$ kPa) to $C_1 = 0.44$ and $C_2 = -0.49$ with $P_M > 0$ (e.g., $P_M = 0.8$ kPa) accompanying with the exchanges of the corresponding eigenmodes.

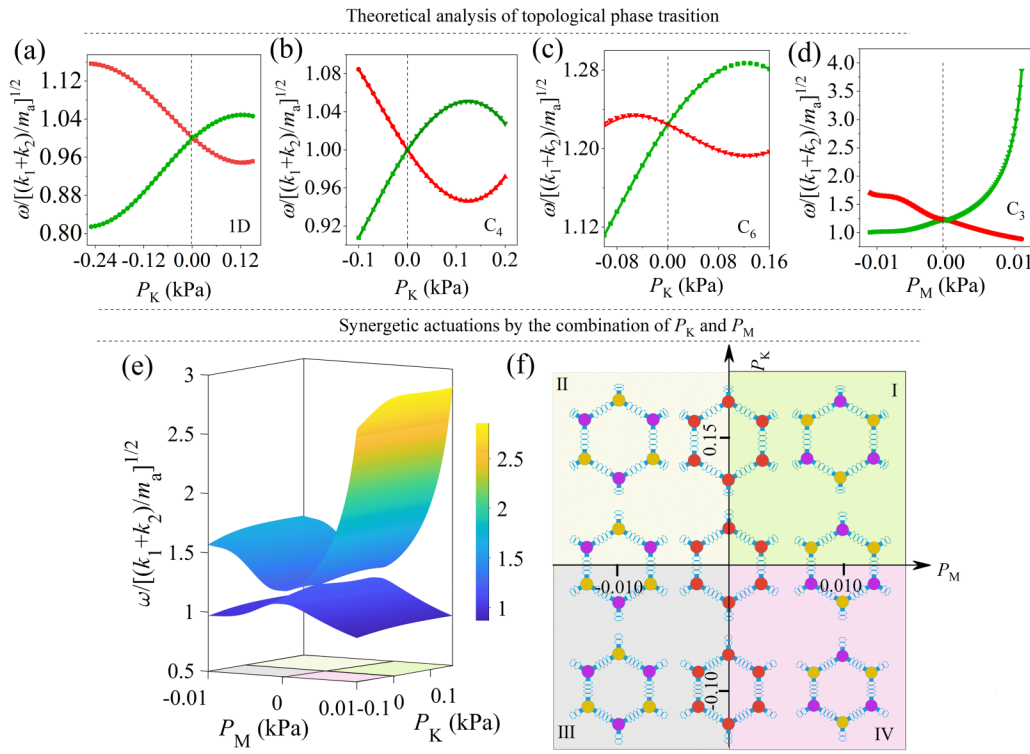


FIG. 4. Active theoretical analysis of topological transitions. (a)–(d) The topological transitions of the 1D, C₄, C₆, and C₃ unit cells calculated in the active spring-mass models. (e) The active switching of the degeneracy DPs in the entire spaces of P_K and P_M. (f) The phase diagram of the active stiffness and mass under the synergistic actuation of pressure P_K and P_M. Specifically, the quantum spin Hall effect and quantum valley Hall effect can be achieved with (P_K ≠ 0, P_M ≡ 0) and (P_M ≠ 0, P_K ≡ 0), respectively.

$$d_x = -k_1(P_K) - k_2(P_K)\cos(a k_x), \quad (13)$$

$$d_y = -k_2(P_K)\sin(a k_x). \quad (14)$$

By inserting Eqs. (10)–(14) into Eq. (9), the winding numbers are W = 1 and W = 0 with P_K < 0 and P_K > 0, respectively. Besides, the first coefficient d₀ is independent of the wave vector k_x, and we just show the relation of the d_x and d_y with k_x ∈ [−π/a, π/a]. Figure 3(b) gives the entire phase diagram of d_x and d_y. As the actuation P_K is negative, the black circles are around the original point with (d_x, d_y) = (0, 0), and its winding number is W = 1, which means the unit cell is topological at the time of suction. These circles gradually move to the right regions with increasing P_K. Once P_K is positive, the red circles are away from the original point, and the winding number is W = 0, indicating that the unit cell is trivial in the time of inflation. Therefore, the proposed method can fast and precisely tune the topological and trivial states of the 1D unit cell.

In Fig. 3(c), a similar topological phase transition of the unit cell with C₄ symmetry is also observed by the actuations of P_K (Table V). For instance, there are four eigenmodes at P_K = −0.08 kPa [Fig. 3(d)], and these modes all have a polarization

in the x-direction because of the DP being at X = (π/a, 0) in the first Brillouin zone [Fig. 8(b)]. From the bottom to the top one, the first and second modes become the fourth and third modes when the active pneumatic is P_K = 0.12 kPa. Besides, the third and fourth modes at P_K = −0.08 kPa are also changed to the second and first modes at P_K = 0.12 kPa. The unstable region [Fig. 3(c)] with a small amplitude of |P_K| is caused by the geometric deformation, which does not affect the topological phase transition [Fig. 3(d)].

The bulk polarization $\mathbf{P} = (P_x, P_y)$ is used to define the phase transition of the active quadrupole unit cell, and it is written as¹⁰

$$P_j = \frac{1}{2\pi} \int_{BZ} \text{tr}[A_j] d^2 \mathbf{k}, \quad (j = x, y) \quad (15)$$

where the subscript j denotes the components in the x- and y-direction. (A_j)_{mn} is the Berry connection and is defined as the inner product of i $\bar{\mathbf{u}}_m^T \partial_{k_j} \bar{\mathbf{u}}_n$, where m and n run over all the bands, and $\bar{\mathbf{u}}_n$ is the displacement vector of the corresponding nth eigenfrequency. The topological state with $\mathbf{P} = (0.24, 0.32)$ under the condition P_K < 0 (e.g., P_K = −0.07 kPa, k₁ < k₂), and the trivial state with $\mathbf{P} = (0, 0)$ under the actuation P_K > 0 (e.g., P_K = +0.06 kPa, k₁ > k₂).¹⁷⁴

In Fig. 3(e), owing to the double degeneracy at the DPs in the C_6 unit cell, there are four eigenmodes at each point of P_K . For instance, the $\mathbf{P}_{1,2}(\mathbf{d}_{1,2})$ modes of the lower (higher) frequencies at $P_K = -0.08$ kPa become the $\mathbf{d}_{1,2}(\mathbf{P}_{1,2})$ modes of the higher (lower) frequencies at $P_K = 0.16$ kPa, where $\mathbf{P}_{1,2}$ and $\mathbf{d}_{1,2}$ are the linear polarization and centrosymmetry. This topological phase transition can be described by the Chern number defined as

$$C_n = \frac{1}{2\pi i} \int_{\Omega} \mathbf{F} d^2 \mathbf{k}, \quad (16)$$

where n is the index of the band and the integral element $\mathbf{F} = \nabla \times \mathbf{A}$ is the Berry curvature.

First, we can obtain the distributions of the Berry curvatures of different bands [Fig. 12 in Appendix B].^{85,175} Then, the Chern number of the n th band can be obtained by integrating Eq. (16) over the Brillouin zone Ω [Fig. 8(e)].^{6,84,173} When the active pneumatic pressure $P_K < 0$ (e.g., $P_K = -0.05$ kPa, $k_1 < k_2$), the Chern numbers are $C_1 = 1.0$, $C_2 = -1.0$, $C_3 = 0.98$, and $C_4 = -0.99$ (the theoretical results are $C_{1,2} = \pm 1$ and $C_{3,4} = \mp 1$). Once the pneumatic is $P_K > 0$ (e.g., $P_K = -0.05$ kPa, $k_1 > k_2$), the Chern numbers are $C_1 = 0$, $C_2 = 0$, $C_3 = 0.0057$, and $C_4 = 0.029$, and they are close to the theoretical result $C = 0$. This result denotes whether the unit cell is topological or trivial under the actuation of suction or inflation.

In Fig. 3(f), at the K point in the Brillouin zone [Fig. 8(h)], the eigenmodes of the opening DPs show a similar topological phase transition to the above cases. We can find that the linear (blue arrow) and rotational (red arrow) eigenmodes of the first and second eigenfrequencies at $P_M = -0.01$ kPa become the eigenmodes of the second and first eigenfrequencies at $P_M = 0.01$ kPa. Similarly, the Chern numbers of the eigenfrequencies change from $C_1 = -0.43$, $C_2 = 0.49$ to $C_1 = 0.44$, $C_2 = -0.49$ (the theoretical results⁶⁹ are $C_{1,2} = \pm 1/2$), with the change of P_M from negative to positive values. The mesh number of the discretized Brillouin zone may result in slight errors between the numerical Chern number and the corresponding theoretical integers.

The above analysis shows that the proposed active strategy provides a facile and effective method to drive the topological phase transition in both 1D and 2D systems. Besides, we can also further extend this method. For example, in Figs. 4(e) and 4(f), the synergetic actuators of P_K and P_M in the C_6 structures are feasible. At the point ($P_K = 0$, $P_M = 0$), the degeneracy takes place, and they are divided into four quadrants. In each quadrant, it has the actuators of I (P_K+ , P_M+), II (P_K+ , P_M-), III (P_K- , P_M-), and IV (P_K- , P_M+), respectively. This synergetic method can not only degrade to the cases of QSHE (P_K -on, P_M -off) and QVHE (P_K -off, P_M -on), but also extend the design space of the active elastic topological insulators.

V. ACTIVE BULK-BOUNDARY EFFECTS

The topological and trivial states of the active composite unit cells are examined in Sec. IV. In this part, a 1D periodic interface is first constructed by the actuation of the programmable air chambers in a 2D system. Later, some exceptional bulk-boundary effects

of the dispersion spectrums,^{7–9,12,18} such as QSHE and QVHE, are uncovered by numerical calculations.

In Fig. 5(a), a 2D superstructure composed of six quadrupole unit cells in the y -direction is constructed at their initial states with $P_K = 0$, and it has a 1D period along the direction a_1 [Fig. 10(a) in Appendix B] with the crystal constant a . All unit cells are divided into a purple and yellow region [Fig. 5(a)], and the unit cells in the purple and yellow regions are driven by $P_K > 0$ and $P_K < 0$, respectively. We can find that the displacements in the x -direction of the masses around the interface have a distinct difference [Fig. 5(a)]. Therefore, a 1D periodic interface is actively constructed between the trivial (purple region) and topological (yellow region) unit cells. Similarly, a periodic interface along the direction a_{K1} [Fig. 10(d) in Appendix B] is also achieved [Fig. 5(b)] with the combination of the C_6 unit cells, and the air chambers in the purple and yellow regions are actuated with $P_K > 0$ and $P_K < 0$, respectively. In the third example [Fig. 5(c)], by making inflation and suction for the vertex masses in the purple and yellow regions, we obtain a 1D periodic interface along the direction a_{M1} [Fig. 10(f) in Appendix B]. Since the air chambers of the unit cell can be actively programmed, the 1D periodic interface can flexibly move along the y -direction.

Further, active pneumatic pressures $P_K = -0.08$ kPa (purple region) and 0.14 kPa (yellow region) are taken to drive the occurrence of the 1D interface, as shown in Fig. 5(a). After the geometric deformations are calculated, the eigenanalysis is performed by applying the Bloch periodic boundary condition on each side of the superstructure along the x -direction and by keeping free boundary conditions on the top and bottom surfaces. The 1D Brillouin zone is discretized into 20 subintervals, and this structure contains 21 eigenanalysis in total. Figure 5(d) shows the dispersion spectrum that has the edge and bulk regions. The yellow color curve in the spectrum is the boundary state, and the eigenmode of the boundary eigenfrequency point at $k_x = 2\pi/(5a)$ (white circle) has a concentrated energy distribution at the 1D periodic interface [Fig. 5(a)]. Interestingly, the eigenmodes of the eigenfrequency points located at the highlighted bulk regions [Fig. 5(d)] have disorder energy distributions in the entire structure. This exceptional boundary-bulk effect provides an effective route for energy transmission and can be fast manipulated by the proposed pneumatic strategy. The white curves [Fig. 5(d)] located out of the highlighted regions may disappear if the mass distances in the structure [Fig. 5(a)] become large enough.

In Fig. 5(e), we take the driving pneumatic pressures $P_K = 0.16$ and -0.1 kPa in the yellow and purple regions in Fig. 5(b). Similarly, after performing the eigenanalysis in the discretized Brillouin zone [Fig. 5(e)], the dispersion curves corresponding to the bulk and boundary cases are given. Unlike the single boundary curve in Fig. 5(d), the blue and red boundary curves [Fig. 5(e)] have different features in their eigenmodes. For details, the boundary points at $k_x = -\pi/5/|a_{K1}|$ (white circle) and $\pi/5/|a_{K1}|$ (white circle) have four eigenmodes, as shown in Figs. 5(g) and 5(h). Clearly, the clockwise (blue arrow) and anticlockwise (red arrow) rotations of the mass displacements in the white boxes show the features of “spin-down” and “spin-up,” which are the prominent feature of the QSHE for the energy transmission at the 1D interface [Fig. 5(b)].^{7–9,12,18}

In Fig. 5(f), the dispersion spectrum is calculated under the actuating air pressures $P_M = 0.01$ and -0.011 kPa in the purple and

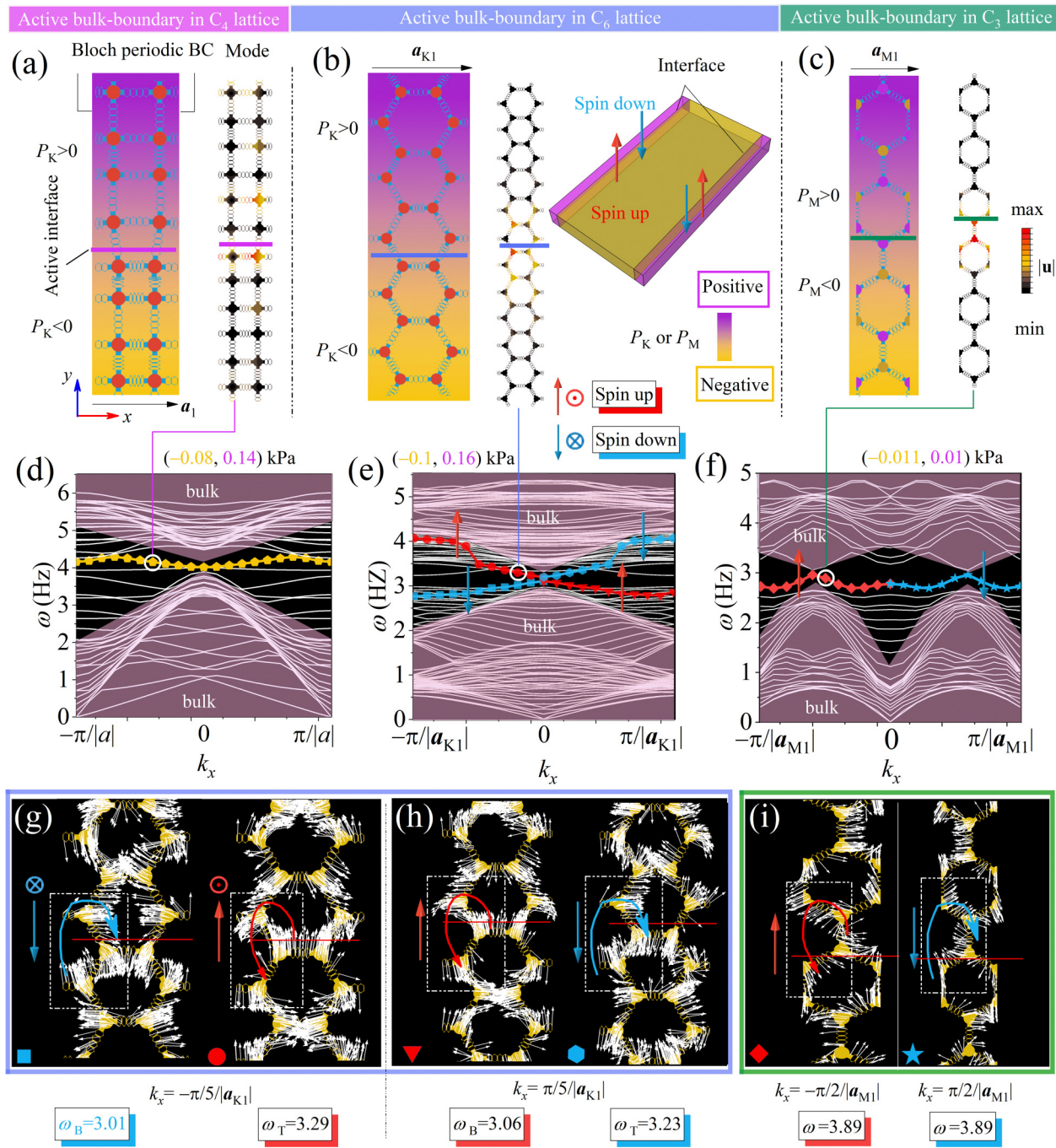


FIG. 5. Active bulk-boundary effects. (a) The active 1D periodic interface is achieved by the programmable actuations $P_K < 0$ (yellow region) and $P_K > 0$ (purple region) for the C_4 unit cells. (b) The active 1D periodic interface is achieved by the programmable actuations $P_K < 0$ (yellow region) and $P_K > 0$ (purple region) for the C_6 unit cells. (c) The active 1D periodic interface is achieved by the programmable actuations $P_M < 0$ (yellow region) and $P_M > 0$ (purple region) for the C_3 unit cells. (d) Dispersion curves of the structure in (a) are calculated with $P_K = -0.08$ kPa and $P_K = 0.14$ kPa. The yellow color is the edge state. (e) Structure in (b) is driven by $P_K = -0.1$ kPa (purple region) and $P_K = 0.16$ kPa (yellow region). The dispersion curves have red and blue spinning edge states. (f) The dispersion curves of the structure in (c) driven by $P_M = -0.011$ kPa (purple region) and $P_M = 0.01$ kPa (yellow region), respectively. (g) and (h) The eigenmodes of the edge points in (e). (i) The eigenmodes of the edge points in (f). The red and blue arrows represent the rotational directions of the masses marked by the white-dotted boxes in (g)–(i).

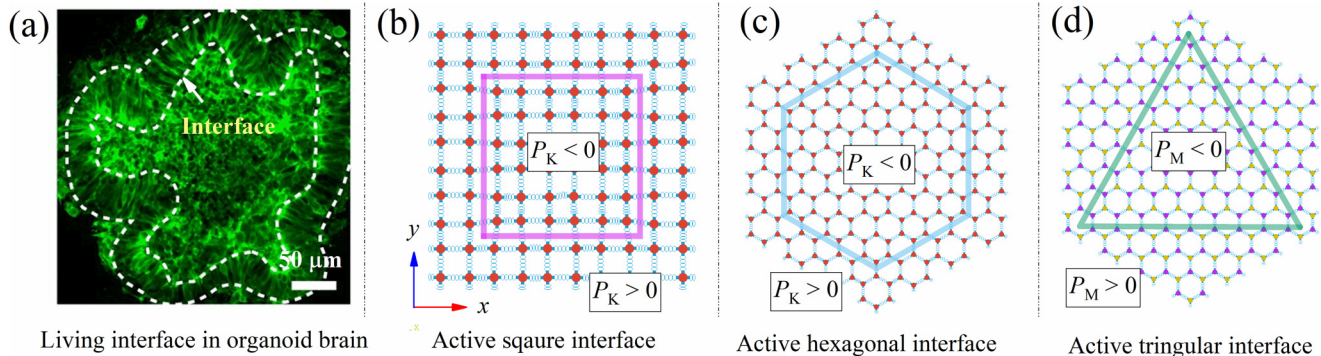


FIG. 6. Active complex interfaces. (a) A living interface in organoids.¹⁸⁴ Reproduced with permission from Karzbrun *et al.*, Nat. Phys. **14**, 515–522 (2018). Copyright 2021 Nature Springer. (b) Active square, (c) hexagonal, and (d) triangular interfaces are constructed by the actuations of P_K or P_M . They are $P_K = (-0.08, 0.14 \text{ kPa})$, $P_K = (-0.1, 0.16 \text{ kPa})$, and $P_M = (-0.11, 0.10 \text{ kPa})$, respectively.

yellow regions. The bulk regions have a peak-valley shape that is separated by a boundary curve. Similarly, the point at the boundary curve also obtains spinning eigenmodes [Fig. 5(i)] and a high energy concentration at the interface [Fig. 5(c)]. Besides, the peak-valley shape can be seen as a new freedom of pseudospin [Fig. 4(f)], which is consistent with the QVHE.^{61,63,74,79,155,176,177}

Together, this section demonstrates the features of the energy distributions and eigenmodes of the 1D periodic active interfaces manipulated by the pneumatic strategy. The exceptional

bulk-boundary effects, including the QSHE and QVHE, are uncovered using the proposed active method.

VI. ACTIVE HIGHER-ORDER TOPOLOGICAL STATES

The 2D topological insulators can transfer energy along the edge or interface with little loss. In recent years, another energy transferring mode that transfers energy through the corners of the 2D or 3D topological materials is uncovered.^{13,16,178} The corner

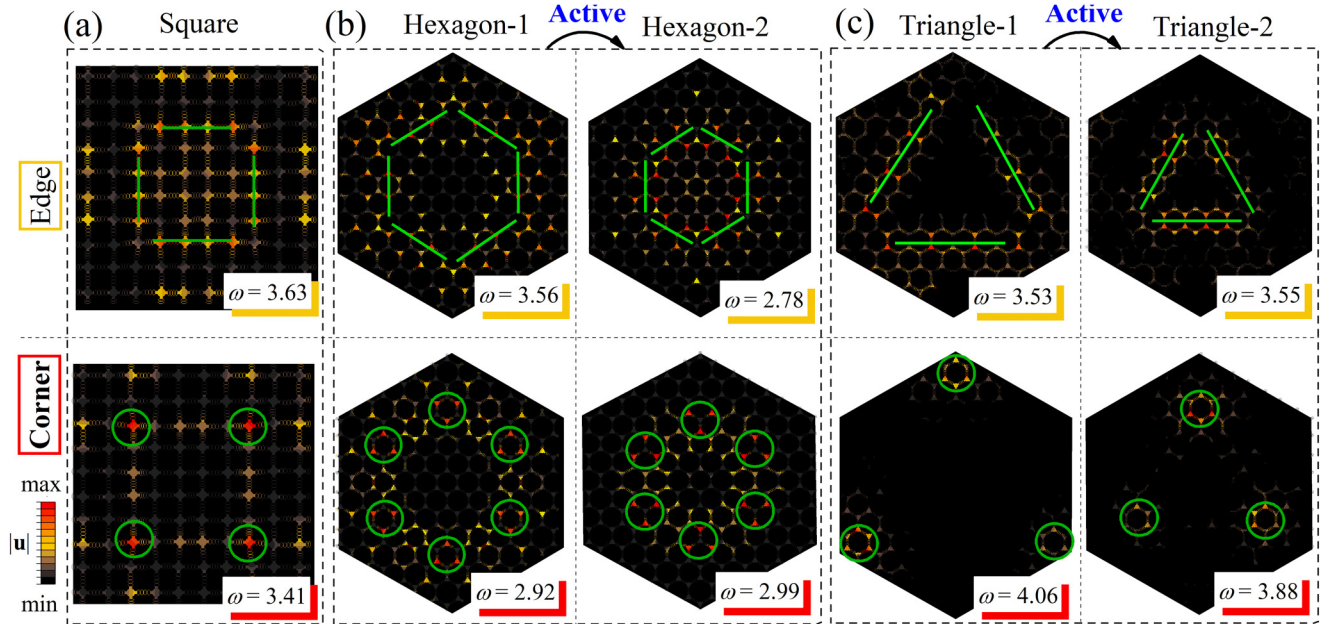


FIG. 7. Edge or corner eigenmodes of the superstructures shown in Fig. 6. (a) Active square interface. (b) Active interfaces that can scale from hexagon-1 to hexagon-2 by the programmed actuation P_K . (c) Active interfaces that can scale from triangle-1 to triangle-2 by the programmed actuation P_M . The green lines and circles denote the first and higher (second) order states.

state of the 2D ($d = 2$) topological insulator has zero dimension in morphology and second (or higher) order in topology ($n = 2$), and it has lower energy loss compared to the classical 1D and first order edge mode ($n = 1$). In general, a d -dimensional and n -order classical topology insulator ($n < d$, $d > 1$) has $(d-1)$, $(d-2)$, ..., $(d-n-1)$ dimensional gapped boundary states and $(d-n)$ dimensional gapless boundary states.^{13,16,36,38,40,43-45,48,59,62,65,179}

A. Active complex interfaces

Typically, these higher-order topological states occur in a complex interface composed of topological and trivial microstructures. While it is difficult for the passive methods to actively, fast construct these complex interfaces, e.g., the active interfaces of nematic¹⁸⁰⁻¹⁸³ and multicellular systems [Fig. 6(a)].^{184,185} In this section, we take the proposed active pneumatic method to find the higher-order topological states in the 2D systems.

The proposed active method has a powerful capacity to construct an active complex interface in 2D and 3D spaces. For simplicity, we take the actuation P_K and P_M to construct the 2D square [Fig. 6(b)], hexagonal [Fig. 6(c)], and triangular [Fig. 6(d)] interfaces,^{65,170} and they are $P_K = (-0.08$ and 0.14 kPa), $P_K = (-0.10$ and 0.16 kPa), and $P_M = (-0.11$ and 0.10 kPa), respectively.

In Fig. 7, the 1D edge states and 0D higher-order corner states of various active interfaces are uncovered through numerical eigenanalysis. Taking the square interface as an example, around the DP as shown in Figs. 2(e) and 13(a), four edges contain high energy distribution of displacement fields (green lines), except the four corners at the active square interface. This energy transferring mode is the classical topological insulator. Besides, at the four corners of the active square interface, there is a higher energy distribution. These higher-order corner states (green circles) are protected by the higher-order topological invariant $Q_C = 4P_x P_y$,^{13,40,44,186,187} where P_x and P_y are the components of bulk polarization \mathbf{P} . Therefore, the topological and trivial states have the topological invariant $Q_C = 1$ and $Q_C = 0$. Similarly, the edge and corner states in Figs. 7(b) and 7(c) can be obtained through the actuations of P_K or P_M , and their higher-order states are also protected by the corresponding nonzero higher-order topological invariants.^{16,17,36,39,45,60,187}

The transmission from corner to corner reduces the energy dissipation, which provides a new prospect for the design of functional devices. In addition, the active interfaces can actively move through the actuations of the programmed air chambers and liquid metallic chambers, such as the interfaces hexagon-1 to hexagon-2 and interfaces triangle-1 to triangle-2. The proposed pneumatic

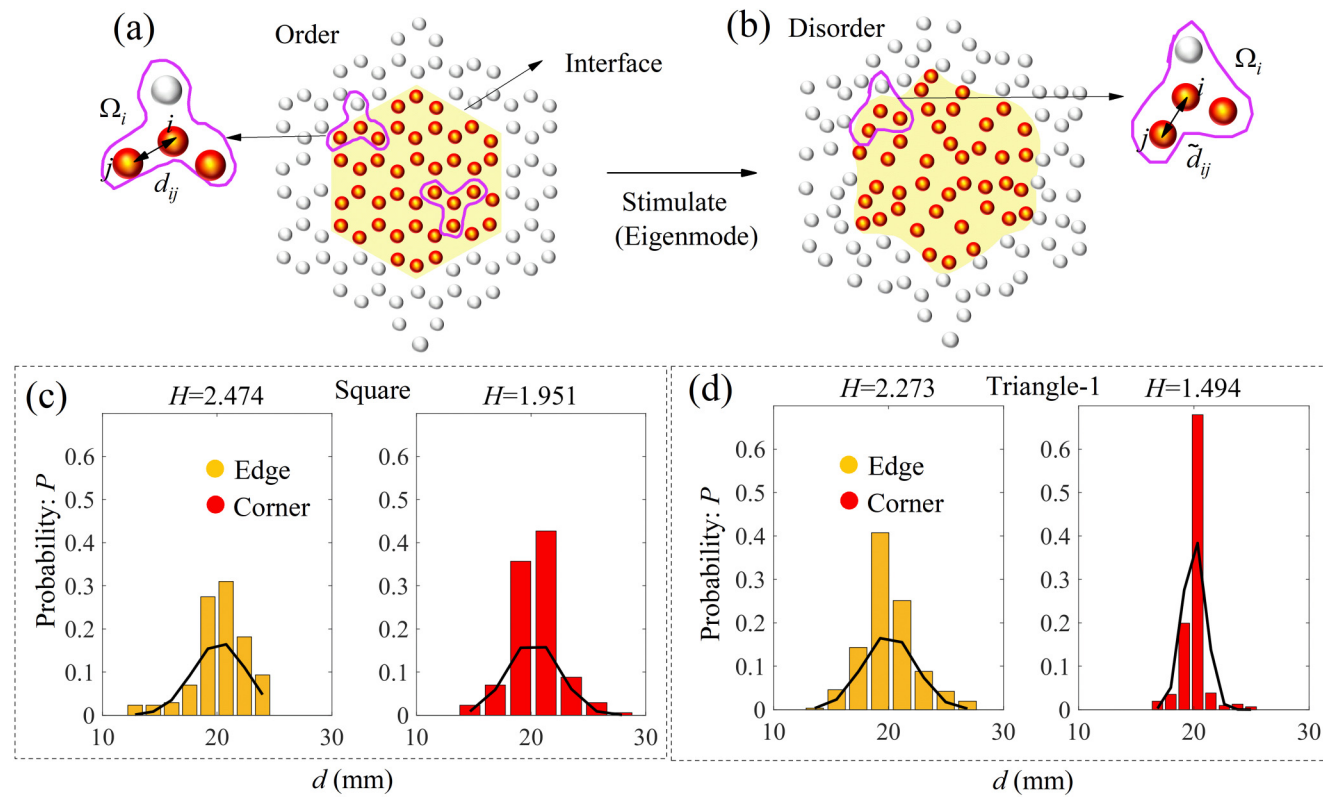


FIG. 8. (a) Superstructure contains ordered particle distributions as shown in Fig. 7, and its disordered eigenmode is shown in (b). (c) Probability distributions and Shannon entropies of the structure in Fig. 7(a). (d) Probability distributions and Shannon entropies of the structure [Fig. 7(c)] that contains the hexagon-1 interface.

TABLE VIII. Statistical average distances (σ) and standard error (δ) of distance.

C ₄ (edge)		C ₄ (corner)		C ₃ (edge)		C ₃ (corner)	
σ (mm)	δ (mm)	σ	δ	σ	δ	σ	δ
20.212	2.358	20.212	2.255	20.074	2.285	20.030	0.994

strategy presents great flexibility for the design of active higher-order topological metamaterials.

B. Information entropy

Further, the higher-order topology invariants cannot unveil the intrinsic and remarkable differences in energy distributions between the 1D edge states and the higher-order 0D corner states for the 2D systems. In Fig. 8, the eigenmodes of the collective mass particles in the superlattices [Fig. 8(a)] can be regarded as a statistical process for the mass locomotion in the eigenanalysis [Fig. 8(b)]. The degree of chaos indicated by the various particle aggregation types can be measured by the information entropy theory.^{107,188}

As examples, we measure the relative distances of metallic chambers of the modes in Fig. 7(a) and the modes (triangle-1) in Fig. 7(c). d_{ij} denotes the distance of each liquid metal cavity i to the liquid metal cavity j in the neighborhood Ω_i [Figs. 8(a) and 8(b)], and the index satisfies $i \in \{1, 2, 3, \dots, N\}$, where N is the total number of metal cavities in the superstructures. In the region Ω_i , there is a connected air chamber between the i and j liquid metal cavities. Finally, all distances d_{ij} are in the interval $[d_{\min}, d_{\max}]$, and then we obtain

$$[d_{\min}, d_{\min} + \delta_d, d_{\min} + 2\delta_d, \dots, d_{\max}], \quad (17)$$

where $\delta_d = (d_{\max} - d_{\min})/N_d$, N_d is the number of discrete copies of the interval. The probability event whose distance falls in the k th ($k \in \{1, 2, 3, \dots, N_d\}$) subinterval in Eq. (17) is denoted as X_k , and its probability is $P(X_k)$. It is obvious to find that there is a clear difference in X_k between the 1D edge state and 0D corner state, and the Shannon entropy is written as

$$H = - \sum_k^{N_d} P(X_k) \log_2 P(X_k). \quad (18)$$

In Figs. 8(c) and 8(d), the information entropy of the 1D edge states is larger than the 0D corner states are $H = 2.474$ and 1.951 for the square interface [Fig. 6(e)] and $H = 2.273$ and 1.494 for the triangular interface. The results show that the higher-order corner states contain lower chaos than the 1D edge states (see the expected values σ and standard errors δ in Table VIII), and this feature is not affected by the geometric shapes of the interfaces. Our finding confirms the advantage of higher-order energy transfer modes.

VII. CONCLUSIONS

In this article, we use the pneumatic actuation method to design elastic topological insulators. This strategy has been

successfully demonstrated to uncover the active topological phase transitions, active bulk-boundary effects, and active higher-order topological states. First, we give the quantitative relation between the connecting stiffness and vertex masses, which vary with respect to the actuators P_K and P_M . To achieve mass exchange, the liquid metal at the lattice vertex can exchange by the actuation of P_M . The dispersion curves of the 1D and 2D (C_4 , C_6 , and C_3) unit cells are calculated under different P_K and P_M . Besides, the opening–closing states of the degeneracy DPs can be precisely and fast manipulated by P_K and P_M , which provides a distinct advantage over the passive methods. Further, the relations between the active topological phase transitions and actuation are systematically uncovered through numerical simulations and theoretical analysis. Furthermore, we have extended this model to uncover the bulk-boundary effects, including the quantum spin and valley hall states, of the 1D periodic interfaces actuated by P_K or P_M . The synergistic actuators P_K and P_M can broaden the design spaces of the topological metamaterials. The proposed method also allows us actively construct complex 2D interfaces, which can achieve higher-order topological corner states. In addition, the Shannon entropy is used to elucidate the formation of the edge and corner states.

The strategy proposed in this work can be extended to design some other, both 2D and 3D, active acoustic and photonic topological insulators. For example, the artificial cylinders obtaining refractive index n_m are taken to design the topological acoustic metamaterials.^{59,189} Through tuning distances of these cylinders, the topological behaviors of acoustic pseudospin multipoles are achieved. Our pneumatic method can actively manipulate the distance of these cylinders. Besides, if the cylinders are composed of dielectric materials, the topological photonic crystals can be achieved.^{60,159}

Finally, it is worth mentioning that the pneumatic strategy is difficult to manipulate active structures at small scales. Therefore, it deserves further theoretical and experimental efforts to design active topological metamaterials and to efficiently perform untethered actuators, which could be achieved by using active cells, magnetic, or other techniques.^{190–192}

ACKNOWLEDGMENTS

Support from the National Natural Science Foundation of China (NNSFC) (Grant No. 11921002) is acknowledged. We also thank the help of Dr. X. Ni from the Photonics Initiative, Advanced Science Research Center, City University of New York and Professor Z. Wang from the Institute for Advanced Study, Tsinghua University. We also thank the help of J. H. Guan from Beijing Academy of Quantum Information Sciences.

AUTHOR DECLARATIONS

Conflict of Interest

The authors have no conflicts to disclose.

Author Contributions

Hui-Kai Zhang: Data curation (equal); Formal analysis (equal); Investigation (equal); Methodology (equal); Resources (equal); Software (equal); Validation (equal); Visualization (equal);

Writing – original draft (equal); Writing – review & editing (equal). **Wei-Tong Chen:** Investigation (equal); Methodology (equal); Writing – review & editing (equal). **Shi-Hao Xu:** Data curation (equal); Investigation (equal); Writing – review & editing (equal). **Jian Wu:** Conceptualization (equal); Supervision (equal); Writing – review & editing (equal). **Bo Li:** Methodology (equal); Visualization (equal); Writing – review & editing (equal). **Xi-Qiao Feng:** Conceptualization (equal); Funding acquisition (equal); Methodology (equal); Project administration (equal); Supervision (equal); Writing – original draft (equal); Writing – review & editing (equal).

DATA AVAILABILITY

The data that support the findings of this study are available from the corresponding author upon reasonable request.

APPENDIX A: EXPERIMENTS AND MATERIALS

In this part, we describe the production process of the multi-chambers [Fig. 1(d)]. It contains the following seven steps [Figs. 9(b) and 9(c)]:

- Print the required mold (PLA material) using a 3D printer (Ultimaker 3);
- Spray a layer of mold release agent RELEASE 200 on the surface of the mold to facilitate later operations;
- Use silicone Dragon Skin 30 to pour the air chamber (or liquid chamber), after combining the chamber part of the mold, pour the evenly mixed uncured silicone Dragon Skin 30, and leave it

for 10 h for the silicone to solidify completely, after demolding, we can get the air chamber (or liquid chamber);

- Use silicone Ecoflex00-30 to pour the intermediate film, pour in the uncured silicone Ecoflex00-30 after uniform mixing and dye it white, let it set for 4 h, then the silicone will be completely solidified. After demolding, we can get the intermediate film;
- Prepare two air chambers (or liquid chambers) and an interlayer film, punch holes in the sides of the two cavities and insert the air tube (2 mm outer diameter, 1 mm inner diameter) and seal the gap with silicone adhesive Sil-pox;
- Apply silicone adhesive Sil-pox to the edges of the two chambers and glue the interlayer film to the opening of one chamber to achieve complete closure;
- Finally, the other chamber is glued in the same way to create a three-layer structure, the corresponding tube of the liquid cavity is clamped with clamps and the liquid metal (gallium-indium alloy, melting point 16 °C) is injected into its interior. Finally, the pinhole is sealed with silicone adhesive Sil-pox.

APPENDIX B: NUMERICAL SIMULATIONS AND ACTIVE THEORETICAL MODELS

1. Finite element method

We use the finite element method to uncover the chamber deformations under pneumatic actuation. The following hyperelastic neo-Hookean constitutive model is used to simulate the silicon

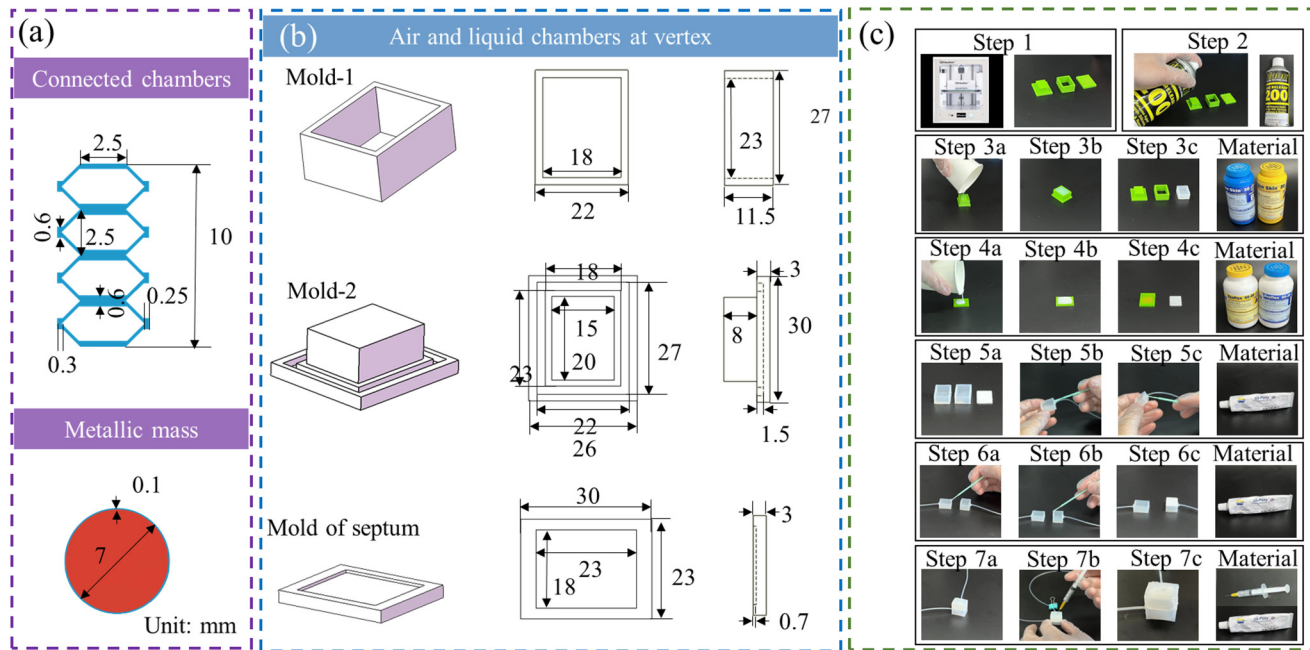


FIG. 9. (a) Geometric parameters of the connected air chambers. (b) gives the structural sizes of the fabricating molds of the vertex air and liquid chambers. (c) The production process of the vertex chambers.

rubber (silicone Ecoflex00-30) of the chambers,¹³³

$$U = C_{10}(\bar{I}_1 - 3) + \frac{1}{D_1}(J^{\text{el}} - 1)^2, \quad (\text{B1})$$

where C_{10} and D_1 are the material parameters and \bar{I}_1 and J^{el} are the first deviatoric invariant and the elastic volume ratio, respectively. In our simulation, the coefficients are set to be $C_{10} = 0.00978$ and $D = 1.0025$ in the commercial software Abaqus, the material density is $\rho_s = 1.05 \times 10^{-3} \text{ g mm}^{-3}$.¹³³

2. Bloch theory

The Bloch periodic theory is taken into the eigenanalysis.¹³³ In the unit cell, the opposite nodal displacements are written as

$$\mathbf{u}(\mathbf{x}_0 + \mathbf{r}) = \mathbf{u}(\mathbf{x}_0) e^{i \mathbf{k} \cdot \mathbf{a}}, \quad (\text{B2})$$

where \mathbf{x}_0 and $\mathbf{x}_0 + \mathbf{r}$ are the coordinates of the opposite edges in the unit cell. \mathbf{a} is the vector of the opposite edge. $\mathbf{r} = \mathbf{a}_x + \mathbf{a}_y$ is the unit directional vector, and $\mathbf{a}_x = a_x \mathbf{e}_x$, where \mathbf{e}_x is the normalized unit basal vector, a_x is the length of the unit cell along the \mathbf{e}_x . $\mathbf{k} = (k_x, k_y)$ is the wave vector in the reciprocal unit cell with its periodic unit vector \mathbf{b} [Figs. 8(b), 8(e), and 8(h)], and it satisfies

$$\mathbf{a}_i \cdot \mathbf{b}_j = 2\pi\delta_{ij} (i, j = 1, 2), \quad (\text{B3})$$

where δ_{ij} is the Kronecker delta. The eigenanalysis is performed in the software Abaqus.

3. Active spring-mass models

Spring-mass model is widely used in the frequency analysis of classical elastic waves. Specifically, it is also used to find the topology effects in the phononic metamaterials based on the tight SSH models. However, the varying mass and coupling stiffness lack real physical properties, which are not controlled by an external actuation. The varying mass strategies, including the rotating gyroscopes, ground frames, and magnetic fluid, are taken into the topological

phononic metamaterial design. However, the varying masses have no explicit relations with the actuation forces. Here, based on Eqs. (1)–(5), the governing equations are obtained by using the Lagrangian equations^{6,84,174,193}

$$\frac{d}{dt} \left(\frac{\partial L}{\partial \dot{\mathbf{u}}} \right) = \frac{\partial L}{\partial \mathbf{u}}. \quad (\text{B4})$$

In what follows, we discuss four cases, which contain the 1D, C_4 , C_6 , and C_3 lattices, respectively.

(1) The governing equations for the 1D active unit cell are

$$\begin{aligned} m_1^{(n)}(P_M) \ddot{u}_1^{(n)} &= -[u_{1(n)} - u_{2(n)}] k_1^{(n)}(P_K) \\ &\quad - [u_{1(n)} - u_{2(n-1)}] k_2^{(n)-(n-1)}(P_K), \end{aligned} \quad (\text{B5})$$

$$\begin{aligned} m_2^{(2)}(P_M) \ddot{u}_2^{(2)} &= -[u_{2(n)} - u_{1(n+1)}] k_2^{(n)-(n+1)}(P_K) \\ &\quad - [u_{2(n)} - u_{1(2)}] k_1^{(n)}(P_K), \end{aligned} \quad (\text{B6})$$

where $P_M = 0$ in Eqs. (B5) and (B6), which indicates $m_1 = m_2 = m_0$, $m_0 = \rho_0 V_0$. $n = 0$ indicates the index of the initial unit cell. By inserting the Bloch periodic boundary $\mathbf{u} = \bar{\mathbf{u}} e^{i(q \mathbf{a}_x \cdot \mathbf{k} - \omega t)}$, where $q \in \{\pm 1, 0\}$, into Eqs. (B5) and (B6), we can obtain the eigenequation

$$\hat{\mathbf{H}}_{2 \times 2} \bar{\mathbf{u}}_{2 \times 1} = \omega^2 \mathbf{M}_{2 \times 2} \bar{\mathbf{u}}_{2 \times 1}, \quad (\text{B7})$$

where

$$\begin{aligned} \hat{\mathbf{H}} &= \begin{bmatrix} k_1(P_K) + k_2(P_K) & -k_1(P_K) - k_2(P_K) e^{-i a_x k_x} \\ -k_1(P_K) - k_2(P_K) e^{i a_x k_x} & k_1(P_K) + k_2(P_K) \end{bmatrix} \text{ and} \\ \mathbf{M} &= \begin{bmatrix} m_1 & 0 \\ 0 & m_2 \end{bmatrix}. \end{aligned} \quad (\text{B8})$$

(2) The active Lagrangian function of the C_4 [Fig. 8(c)] unit cell is

$$\begin{aligned} L(P_K) &= \frac{1}{2} \left[\sum_i^4 m_0 \left(\dot{u}_{i(0,0)}^2 + \dot{v}_{i(0,0)}^2 \right) \right] - \frac{1}{2} \tilde{k}_2 \left[\left(u_{1(0,0)} - u_{4(-1,0)} \right)^2 + \left(v_{1(0,0)} - v_{2(0,1)} \right)^2 \right] - \frac{1}{2} \tilde{k}_2 \left[\left(u_{2(0,0)} - u_{3(-1,0)} \right)^2 + \left(v_{2(0,0)} - v_{1(0,-1)} \right)^2 \right] \\ &\quad - \frac{1}{2} \tilde{k}_2 \left[\left(u_{3(0,0)} - u_{2(1,0)} \right)^2 + \left(v_{3(0,0)} - v_{4(0,-1)} \right)^2 \right] - \frac{1}{2} \tilde{k}_2 \left[\left(u_{4(0,0)} - u_{1(1,0)} \right)^2 + \left(v_{4(0,0)} - v_{3(0,1)} \right)^2 \right] \\ &\quad - \frac{1}{2} \tilde{k}_1 \left[\left(u_{1(0,0)} - u_{4(0,0)} \right)^2 + \left(u_{2(0,0)} - u_{3(0,0)} \right)^2 \right] - \frac{1}{2} \tilde{k}_1 \left[\left(v_{1(0,0)} - v_{2(0,0)} \right)^2 + \left(v_{2(0,0)} - v_{4(0,0)} \right)^2 \right], \end{aligned} \quad (\text{B9})$$

where $\tilde{k}_1 = k_1(P_K)$ and $\tilde{k}_2 = k_2(P_K)$ are the intracell and intercell active stiffness, respectively, and index (p, q) is set as $(0, 0)$. Using the Bloch theory [Fig. 10(c)], we can obtain the governing equations

$$-m_0 \omega^2 \bar{u}_{1(0,0)} = (-\tilde{k}_1 - \tilde{k}_2) \bar{u}_{1(0,0)} + (\tilde{k}_1 + \tilde{k}_2 e^{-i k_x a_x}) \bar{u}_{4(0,0)}, \quad (\text{B10})$$

$$-m_0 \omega^2 \bar{v}_{1(0,0)} = (-\tilde{k}_1 - \tilde{k}_2) \bar{v}_{1(0,0)} + (\tilde{k}_1 + \tilde{k}_2 e^{i k_y a_y}) \bar{v}_{2(0,0)}, \quad (\text{B11})$$

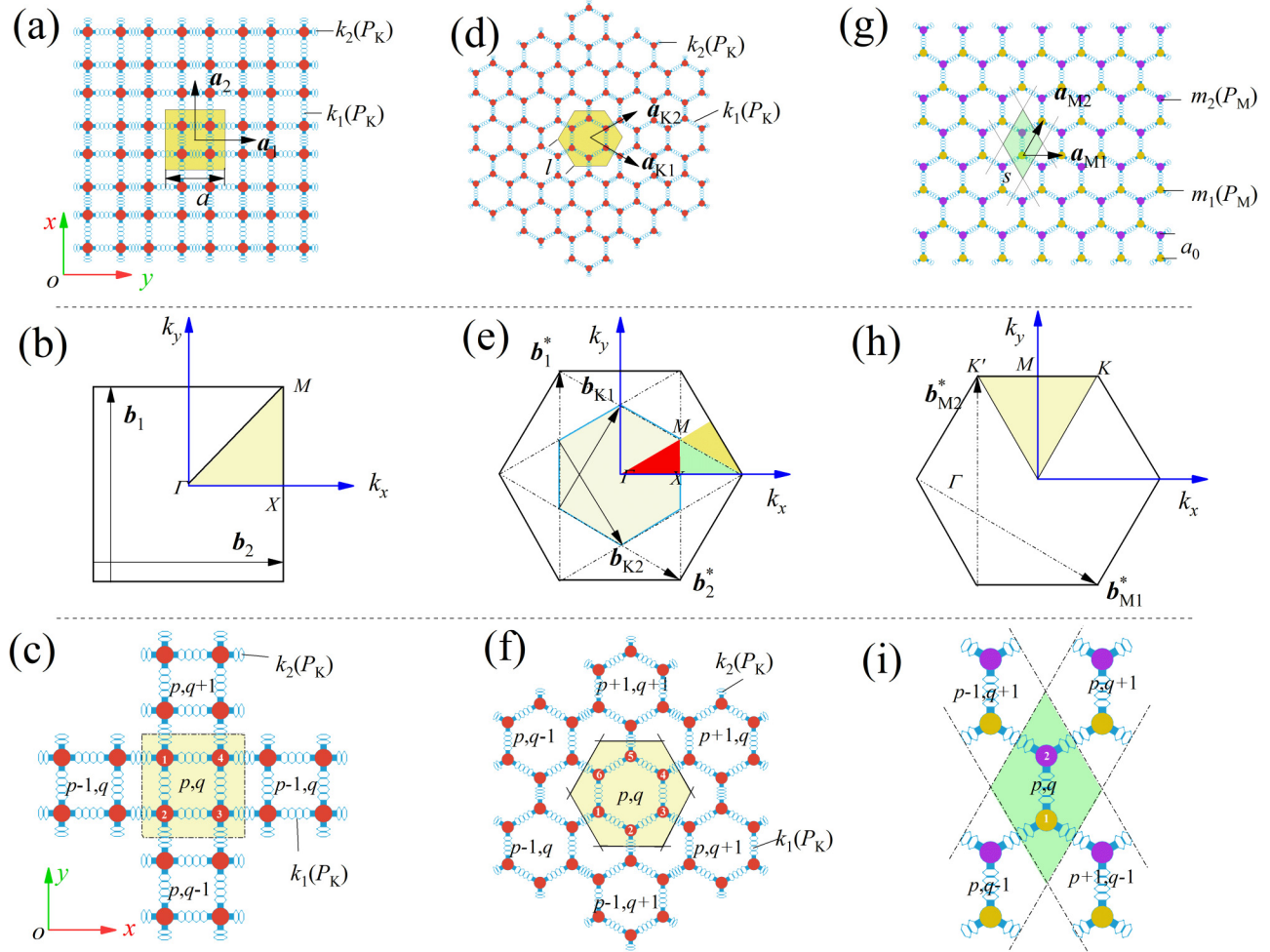


FIG. 10. (a), (d), and (g) Active composite microstructures with C₄, C₆, and C₃ symmetry, and their crystal lengths are a , l , and s , respectively. The crystal vectors in (a) are $\mathbf{a}_1 = a(1, 0)$ and $\mathbf{a}_2 = a(0, 1)$. The crystal vectors in (d) are $\mathbf{a}_{K1} = l(3/2, \sqrt{3}/2)$ and $\mathbf{a}_{K2} = l(3/2, -\sqrt{3}/2)$. The crystal vectors in (g) are $\mathbf{a}_{M1} = a_0(\sqrt{3}, 0)$ and $\mathbf{a}_{M2} = a_0(\sqrt{3}/2, 3/2)$. $a_0 = 20$ mm is the mass distance in (g). (b), (e), and (h) The corresponding Brillouin zones of the C₄, C₆, and C₃ microstructures. (c), (f), and (i) are the Bloch periodic boundary conditions for the 2D active theoretical models.

$$-m_0\omega^2\bar{u}_{2(0,0)} = (-\tilde{k}_1 - \tilde{k}_2)\bar{u}_{2(0,0)} + (\tilde{k}_1 + \tilde{k}_2 e^{-ik_x a_x})\bar{u}_{3(0,0)}, \quad (\text{B12})$$

$$-m_0\omega^2\bar{v}_{2(0,0)} = (-\tilde{k}_1 - \tilde{k}_2)\bar{v}_{2(0,0)} + (\tilde{k}_1 + \tilde{k}_2 e^{-ik_y a_y})\bar{v}_{1(0,0)}, \quad (\text{B13})$$

$$-m_0\omega^2\bar{u}_{3(0,0)} = (-\tilde{k}_1 - \tilde{k}_2)\bar{u}_{3(0,0)} + (\tilde{k}_1 + \tilde{k}_2 e^{ik_x a_x})\bar{u}_{2(0,0)}, \quad (\text{B14})$$

$$-m_0\omega^2\bar{v}_{3(0,0)} = (-\tilde{k}_1 - \tilde{k}_2)\bar{v}_{3(0,0)} + (\tilde{k}_1 + \tilde{k}_2 e^{-ik_y a_y})\bar{v}_{4(0,0)}, \quad (\text{B15})$$

$$-m_0\omega^2\bar{u}_{4(0,0)} = (-\tilde{k}_1 - \tilde{k}_2)\bar{u}_{4(0,0)} + (\tilde{k}_1 + \tilde{k}_2 e^{ik_x a_x})\bar{u}_{1(0,0)}, \quad (\text{B16})$$

$$-m_0\omega^2\bar{v}_{4(0,0)} = (-\tilde{k}_1 - \tilde{k}_2)\bar{v}_{4(0,0)} + (\tilde{k}_1 + \tilde{k}_2 e^{ik_y a_y})\bar{v}_{3(0,0)}. \quad (\text{B17})$$

Then, the eigenequation is

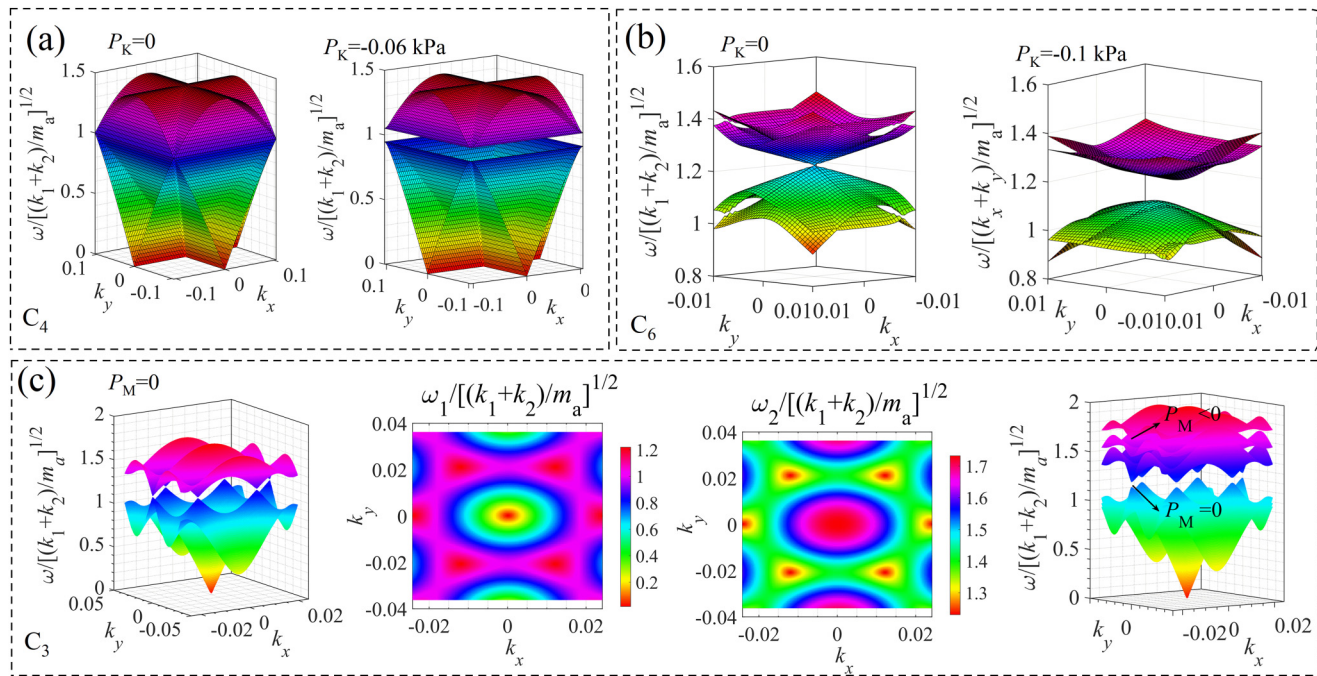
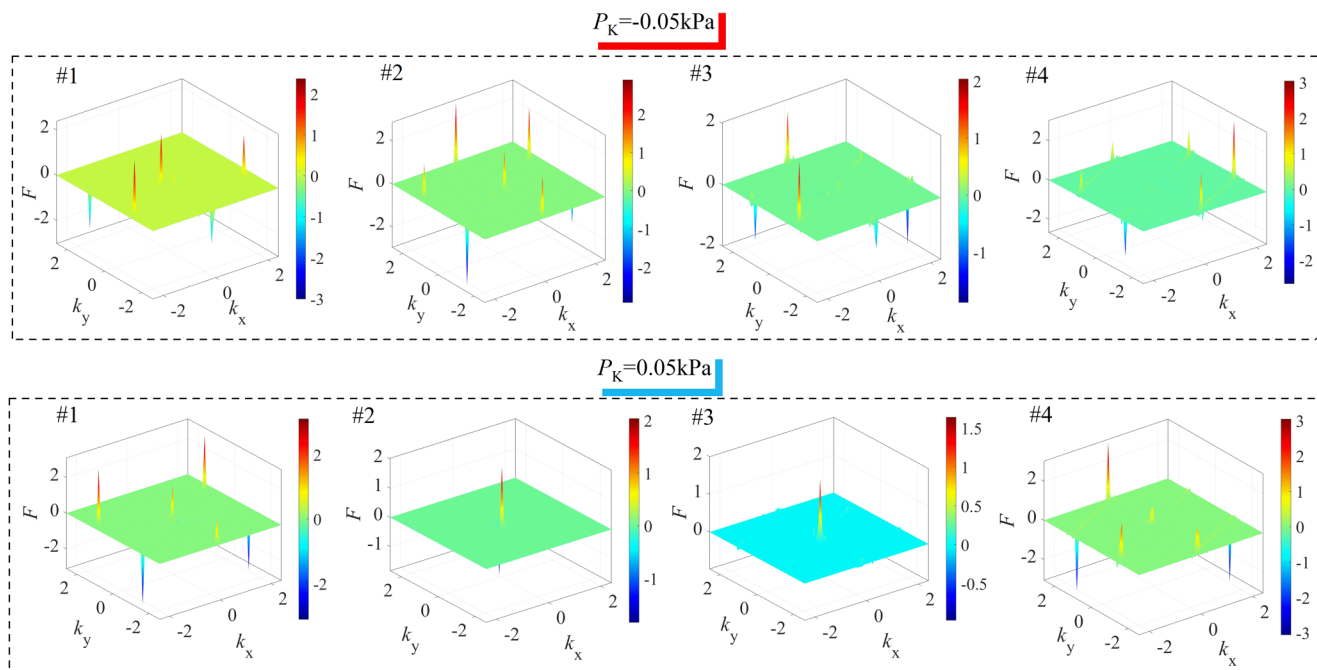
$$\hat{\mathbf{H}}_{8 \times 8} \bar{\mathbf{u}}_{8 \times 1} = \omega^2 \mathbf{M}_{8 \times 8} \bar{\mathbf{u}}_{8 \times 1}, \quad (\text{B18})$$

where $\mathbf{M} = m_0 \mathbf{I}_{8 \times 8}$ is the mass matrix, and $\hat{\mathbf{H}}$ is the active Hamilton matrix, whose elements are

$$\text{diag}(\mathbf{H}) = \tilde{k}_1 + \tilde{k}_2, \quad H_{17} = H_{35} = -\tilde{k}_1 - \tilde{k}_2 e^{-ik_x a_x}, \quad (\text{B19})$$

$$H_{24} = H_{68} = -\tilde{k}_1 - \tilde{k}_2 e^{-ik_y a_y}, \quad H_{71}^\dagger = H_{17}, \quad (\text{B20})$$

$$H_{53}^\dagger = H_{35}, \quad H_{42}^\dagger = H_{24}, \quad H_{86}^\dagger = H_{68}, \quad (\text{B21})$$

FIG. 11. Dispersion surfaces in the entire Brillouin zone for C₄ (a), C₆ (b), and C₃ (c) microstructures under different P_K or P_M.FIG. 12. Berry curvatures under different actuations P_K (C₆ unit cell).

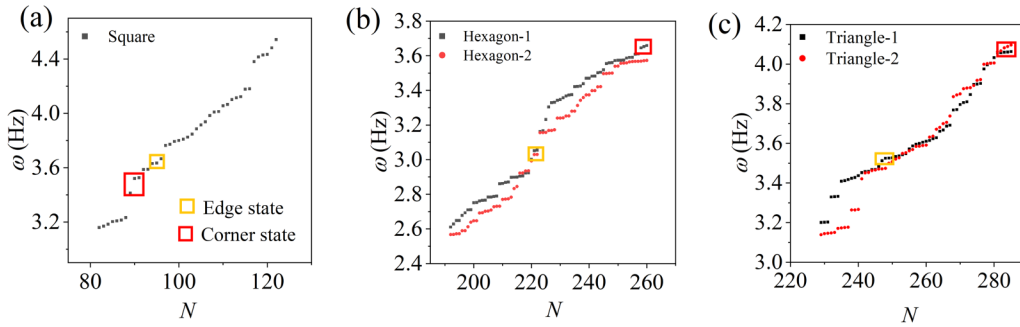


FIG. 13. (a)–(c) Dispersion frequencies correspond to the eigenmodes shown in Figs. 7(a)–7(c). The yellow and red frames denote the edge and corner states, respectively.

where other elements are zero, the symbol “ \dagger ” denotes the conjugate operator, and $a_x = a_y = a$.

(3) The active Lagrangian function of the C_6 unit cell [Fig. 10(f)] is

$$L = \frac{m_1(P_M)}{2} \left[\dot{u}_{1(0,0)}^2 + u_{3(0,0)}^2 + \dot{u}_{5(0,0)}^2 + \dot{v}_{1(0,0)}^2 + v_{3(0,0)}^2 + \dot{v}_{5(0,0)}^2 \right] + \frac{m_2(P_M)}{2} \left[\dot{u}_{2(0,0)}^2 + u_{4(0,0)}^2 + \dot{u}_{6(0,0)}^2 + \dot{v}_{2(0,0)}^2 + v_{4(0,0)}^2 + \dot{v}_{6(0,0)}^2 \right] - \frac{\tilde{k}_2}{2} \{ [\mathbf{u}_{1(0,0)} - \mathbf{u}_{4(0,-1)}] \cdot \mathbf{e}^{1(0,0)-4(0,-1)} \}^2 - \frac{\tilde{k}_2}{2} \{ [\mathbf{u}_{2(0,0)} - \mathbf{u}_{5(-1,0)}] \cdot \mathbf{e}^{2(0,0)-5(-1,0)} \}^2 - \frac{\tilde{k}_2}{2} \{ [\mathbf{u}_{3(0,0)} - \mathbf{u}_{6(-1,1)}] \cdot \mathbf{e}^{3(0,0)-6(-1,1)} \}^2 - \frac{\tilde{k}_2}{2} \{ [\mathbf{u}_{4(0,0)} - \mathbf{u}_{1(0,1)}] \cdot \mathbf{e}^{4(0,0)-1(0,1)} \}^2 - \frac{\tilde{k}_2}{2} \{ [\mathbf{u}_{5(0,0)} - \mathbf{u}_{2(1,0)}] \cdot \mathbf{e}^{5(0,0)-2(1,0)} \}^2 - \frac{\tilde{k}_2}{2} \{ [\mathbf{u}_{6(0,0)} - \mathbf{u}_{3(1,-1)}] \cdot \mathbf{e}^{6(0,0)-3(1,-1)} \}^2 - \frac{\tilde{k}_1}{2} \{ [\mathbf{u}_{1(0,0)} - \mathbf{u}_{2(0,0)}] \cdot \mathbf{e}^{1(0,0)-2(0,0)} \}^2 - \frac{\tilde{k}_1}{2} \{ [\mathbf{u}_{2(0,0)} - \mathbf{u}_{3(0,0)}] \cdot \mathbf{e}^{2(0,0)-3(0,0)} \}^2 - \frac{\tilde{k}_1}{2} \{ [\mathbf{u}_{3(0,0)} - \mathbf{u}_{4(0,0)}] \cdot \mathbf{e}^{3(0,0)-4(0,0)} \}^2 - \frac{\tilde{k}_1}{2} \{ [\mathbf{u}_{4(0,0)} - \mathbf{u}_{5(0,0)}] \cdot \mathbf{e}^{4(0,0)-5(0,0)} \}^2 - \frac{\tilde{k}_1}{2} \{ [\mathbf{u}_{5(0,0)} - \mathbf{u}_{6(0,0)}] \cdot \mathbf{e}^{5(0,0)-6(0,0)} \}^2 - \frac{\tilde{k}_1}{2} \{ [\mathbf{u}_{6(0,0)} - \mathbf{u}_{1(0,0)}] \cdot \mathbf{e}^{6(0,0)-1(0,0)} \}^2, \quad (B22)$$

where $\mathbf{u}_{i(0,0)} = (u_i, v_i)_{(0,0)}$, ($i = 1, 2, \dots, 6$) is the displacement vector of i th vertex mass, and the directional vectors of the active springs are

$$\begin{aligned} \mathbf{e}^{1(0,0)-2(0,0)} &= (0, -1), \quad \mathbf{e}^{2(0,0)-3(0,0)} = \left(\frac{\sqrt{3}}{2}, -\frac{1}{2} \right), \\ \mathbf{e}^{3(0,0)-4(0,0)} &= \left(\frac{\sqrt{3}}{2}, \frac{1}{2} \right), \end{aligned} \quad (B23)$$

$$\begin{aligned} \mathbf{e}^{4(0,0)-1(0,1)} &= \left(\frac{\sqrt{3}}{2}, -\frac{1}{2} \right), \quad \mathbf{e}^{5(0,0)-2(1,0)} = \left(\frac{\sqrt{3}}{2}, \frac{1}{2} \right), \\ \mathbf{e}^{6(0,0)-3(1,-1)} &= (0, 1). \end{aligned} \quad (B26)$$

Similarly, 12 governing equations of the C_6 unit cell are

$$\mathbf{e}^{4(0,0)-5(0,0)} = (0, 1), \quad \mathbf{e}^{5(0,0)-6(0,0)} = \left(-\frac{\sqrt{3}}{2}, \frac{1}{2} \right), \quad (B24)$$

$$\mathbf{e}^{6(0,0)-1(0,0)} = \left(-\frac{\sqrt{3}}{2}, -\frac{1}{2} \right),$$

$$\mathbf{e}^{1(0,0)-4(0,-1)} = \left(-\frac{\sqrt{3}}{2}, \frac{1}{2} \right), \quad \mathbf{e}^{2(0,0)-5(-1,0)} = \left(-\frac{\sqrt{3}}{2}, -\frac{1}{2} \right), \quad (B25)$$

$$\mathbf{e}^{3(0,0)-6(-1,1)} = (0, -1),$$

$$\begin{aligned} m_1 \ddot{u}_{1(0,0)}^2 &= \left(-\frac{3}{4} \tilde{k}_2 - \frac{3}{4} \tilde{k}_1 \right) u_{1(0,0)} + \left(\frac{\sqrt{3}}{4} \tilde{k}_2 - \frac{\sqrt{3}}{4} \tilde{k}_1 \right) v_{1(0,0)} \\ &\quad + \frac{3}{4} \tilde{k}_2 u_{4(0,-1)} - \frac{\sqrt{3}}{4} \tilde{k}_2 v_{4(0,-1)} + \frac{3}{4} \tilde{k}_1 u_{6(0,0)} \\ &\quad + \frac{\sqrt{3}}{4} \tilde{k}_1 v_{6(0,0)}, \end{aligned} \quad (B27)$$

$$m_1 \dot{v}_{1(0,0)}^2 = \left(\frac{\sqrt{3}}{4} \tilde{k}_2 - \frac{\sqrt{3}}{4} \tilde{k}_1 \right) u_{1(0,0)} + \left(-\frac{\tilde{k}_2}{4} - \frac{5}{4} \tilde{k}_1 \right) v_{1(0,0)} + \tilde{k}_1 v_{2(0,0)} \\ - \frac{\sqrt{3}}{4} \tilde{k}_2 u_{4(0,-1)} + \frac{\tilde{k}_2}{4} v_{4(0,-1)} + \frac{\sqrt{3}}{4} \tilde{k}_1 u_{6(0,0)} + \frac{\tilde{k}_1}{4} v_{6(0,0)}, \quad (\text{B28})$$

$$m_2 \dot{u}_{2[0,0]}^2 = \left(-\frac{3}{4} \tilde{k}_2 - \frac{3}{4} \tilde{k}_1 \right) u_{2(0,0)} + \left(\frac{\sqrt{3}}{4} \tilde{k}_1 - \frac{\sqrt{3}}{4} \tilde{k}_2 \right) v_{2(0,0)} \\ + \frac{3}{4} \tilde{k}_1 u_{3(0,0)} - \frac{\sqrt{3}}{4} \tilde{k}_1 v_{3(0,0)} + \frac{\sqrt{3}}{4} \tilde{k}_2 u_{5(-1,0)} + \frac{\sqrt{3}}{4} \tilde{k}_2 v_{5(-1,0)}, \quad (\text{B29})$$

$$m_2 \dot{v}_{2(0,0)}^2 = k_1 v_{1(0,0)} + \left(\frac{\sqrt{3}}{4} \tilde{k}_1 - \frac{\sqrt{3}}{4} \tilde{k}_2 \right) u_{2(0,0)} + \left(-\frac{5}{4} \tilde{k}_1 - \frac{\tilde{k}_2}{4} \right) v_{2(0,0)} \\ - \frac{\sqrt{3}}{4} \tilde{k}_1 u_{3(0,0)} + \frac{\tilde{k}_1}{4} v_{3(0,0)} + \frac{\sqrt{3}}{4} \tilde{k}_2 u_{5(-1,0)} + \frac{\tilde{k}_2}{4} v_{5(-1,0)}, \quad (\text{B30})$$

$$m_1 \dot{u}_{3(0,0)}^2 = \frac{3}{4} \tilde{k}_1 u_{2(0,0)} - \frac{\sqrt{3}}{4} \tilde{k}_1 v_{2(0,0)} - \frac{3}{2} \tilde{k}_1 u_{3(0,0)} + \frac{3}{4} \tilde{k}_1 u_{4(0,0)} \\ + \frac{\sqrt{3}}{4} \tilde{k}_1 v_{4(0,0)}, \quad (\text{B31})$$

$$m_1 \dot{v}_{3[0,0]}^2 = -\frac{\sqrt{3}}{4} \tilde{k}_1 u_{2(0,0)} + \frac{\tilde{k}_1}{4} v_{2(0,0)} + \left(-\tilde{k}_2 - \frac{\tilde{k}_1}{2} \right) v_{3(0,0)} \\ + \frac{\sqrt{3}}{4} \tilde{k}_1 u_{4(0,0)} + \frac{\tilde{k}_1}{4} v_{4(0,0)} + \tilde{k}_2 v_{6(-1,1)}, \quad (\text{B32})$$

$$m_2 \dot{u}_{4(0,0)}^2 = \frac{3}{4} \tilde{k}_2 u_{1(0,0)} - \frac{\sqrt{3}}{4} \tilde{k}_2 v_{1(0,1)} + \frac{3}{4} \tilde{k}_1 u_{3(0,0)} + \frac{\sqrt{3}}{4} \tilde{k}_1 v_{3(0,0)} \\ + \left(-\frac{3}{4} \tilde{k}_2 - \frac{3}{4} \tilde{k}_1 \right) u_{4(0,0)} + \left(\frac{\sqrt{3}}{4} \tilde{k}_2 - \frac{\sqrt{3}}{4} \tilde{k}_1 \right) v_{4(0,0)}, \quad (\text{B33})$$

$$m_2 \dot{v}_{4(0,0)}^2 = -\frac{\sqrt{3}}{4} \tilde{k}_2 u_{1(0,1)} + \frac{\tilde{k}_2}{4} v_{1(0,1)} + \frac{\sqrt{3}}{4} \tilde{k}_1 u_{3(0,0)} + \frac{\tilde{k}_1}{4} v_{3(0,0)} \\ + \left(\frac{\sqrt{3}}{4} \tilde{k}_2 - \frac{\sqrt{3}}{4} \tilde{k}_1 \right) u_{4(0,0)} + \left(-\frac{\tilde{k}_2}{4} - \frac{5}{4} \tilde{k}_1 \right) v_{4(0,0)} \\ + \tilde{k}_1 v_{5(0,0)}, \quad (\text{B34})$$

$$m_1 \dot{u}_{5(0,0)}^2 = \frac{3}{4} \tilde{k}_2 u_{2(1,0)} + \frac{\sqrt{3}}{4} \tilde{k}_2 v_{2(1,0)} + \left(-\frac{3}{4} \tilde{k}_2 - \frac{3}{4} \tilde{k}_1 \right) u_{5(0,0)} \\ + \left(\frac{\sqrt{3}}{4} \tilde{k}_1 - \frac{\sqrt{3}}{4} \tilde{k}_2 \right) v_{5(0,0)} + \frac{\sqrt{3}}{4} \tilde{k}_1 u_{6(0,0)} - \frac{\sqrt{3}}{4} \tilde{k}_1 v_{6(0,0)}, \quad (\text{B35})$$

$$m_1 \dot{v}_{5(0,0)}^2 = \frac{\sqrt{3}}{4} \tilde{k}_2 u_{2(1,0)} + \frac{\tilde{k}_2}{4} v_{2(1,0)} + \tilde{k}_1 v_{4(0,0)} + \left(-\frac{\sqrt{3}}{4} \tilde{k}_2 + \frac{\sqrt{3}}{4} \tilde{k}_1 \right) u_{5(0,0)} \\ + \left(-\frac{\tilde{k}_2}{4} - \frac{5}{4} \tilde{k}_1 \right) v_{5(0,0)} - \frac{\sqrt{3}}{4} \tilde{k}_1 u_{6(0,0)} + \frac{\tilde{k}_1}{4} v_{6(0,0)}, \quad (\text{B36})$$

$$m_2 \dot{u}_{6(0,0)}^2 = \frac{3}{4} \tilde{k}_1 u_{1(0,0)} + \frac{\sqrt{3}}{4} \tilde{k}_1 v_{1(1,0)} + \frac{3}{4} \tilde{k}_1 u_{5(0,0)} \\ - \frac{\sqrt{3}}{4} \tilde{k}_1 v_{5(0,0)} - \frac{3}{2} \tilde{k}_1 u_{(0,0)}, \quad (\text{B37})$$

$$m_2 \dot{v}_{6(0,0)}^2 = \frac{\sqrt{3}}{4} \tilde{k}_1 u_{1(0,0)} + \frac{\tilde{k}_1}{4} v_{1(0,0)} + \tilde{k}_2 v_{3(1,-1)} \\ - \frac{\sqrt{3}}{4} \tilde{k}_1 u_{5(0,0)} + \frac{\tilde{k}_1}{4} v_{5(0,0)} + \left(-\tilde{k}_2 - \frac{\tilde{k}_1}{2} \right) v_{6(0,0)}. \quad (\text{B38})$$

By combining the periodic Bloch theory $\mathbf{u} = \bar{\mathbf{u}} e^{i[\mathbf{k} \cdot (p \mathbf{a}_{K1} + q \mathbf{a}_{K2}) - \omega t]}$, where $p, q \in \{\pm 1, 0\}$, and the crystal vectors in (d) are $\mathbf{a}_{K1} = l(3/2, \sqrt{3}/2)$ and $\mathbf{a}_{K2} = l(3/2, -\sqrt{3}/2)$. Equations (B27)–(B38) can be written as

$$[\mathbf{H}_{12 \times 12}(P_K) + \omega^2 \mathbf{M}_{12 \times 12}] \bar{\mathbf{u}}_{12 \times 1} = \mathbf{0}, \quad (\text{B39})$$

where $\mathbf{H}(P_K)$ is the active Hamilton matrix. All the components are written as

$$H_{1,1} = -\frac{3}{4} \tilde{k}_2 - \frac{3}{4} \tilde{k}_1, \quad H_{1,2} = \frac{\sqrt{3}}{4} \tilde{k}_2 - \frac{\sqrt{3}}{4} \tilde{k}_1, \quad H_{1,7} = \frac{3}{4} \tilde{k}_2 e^{i[\mathbf{k} \cdot (-\mathbf{a}_{K2})]}, \\ H_{1,8} = -\frac{\sqrt{3}}{4} \tilde{k}_2 e^{i[\mathbf{k} \cdot (-\mathbf{a}_{K2})]}, \quad H_{1,11} = \frac{3}{4} \tilde{k}_1, \quad H_{1,12} = \frac{\sqrt{3}}{4} \tilde{k}_1, \quad (\text{B40})$$

$$H_{2,1} = H_{1,2}, \quad H_{2,2} = -\frac{\tilde{k}_2}{4} - \frac{5}{4} \tilde{k}_1, \quad H_{2,4} = \tilde{k}_1, \quad H_{2,7} = -\frac{\sqrt{3}}{4} \tilde{k}_2 e^{i[\mathbf{k} \cdot (-\mathbf{a}_{K2})]} \\ H_{2,8} = \frac{\tilde{k}_2}{4} e^{i[\mathbf{k} \cdot (-\mathbf{a}_{K2})]}, \quad H_{2,11} = \frac{\sqrt{3}}{4} \tilde{k}_1, \quad H_{2,12} = \frac{\tilde{k}_1}{4}; \quad (\text{B41})$$

$$H_{3,3} = H_{1,1}, \quad H_{3,4} = \frac{\sqrt{3}}{4} \tilde{k}_1 - \frac{\sqrt{3}}{4} \tilde{k}_2, \quad H_{3,5} = \frac{3}{4} \tilde{k}_1, \\ H_{3,6} = -\frac{\sqrt{3}}{4} \tilde{k}_1, \quad H_{3,9} = \frac{3}{4} \tilde{k}_2 e^{i[\mathbf{k} \cdot (-\mathbf{a}_{K1})]}, \quad H_{3,10} = \frac{\sqrt{3}}{4} \tilde{k}_2 e^{i[\mathbf{k} \cdot (-\mathbf{a}_{K1})]}, \quad (\text{B42})$$

$$H_{4,2} = H_{2,4}, \quad H_{4,3} = H_{3,4}, \quad H_{4,4} = H_{2,2}, \quad H_{4,5} = -\frac{\sqrt{3}}{4} \tilde{k}_1, \\ H_{4,6} = \frac{\tilde{k}_1}{4}, \quad H_{4,9} = \frac{\sqrt{3}}{4} \tilde{k}_2 e^{i[\mathbf{k} \cdot (-\mathbf{a}_{K1})]}, \quad H_{4,10} = \frac{\tilde{k}_2}{4} e^{i[\mathbf{k} \cdot (-\mathbf{a}_{K1})]}, \quad (\text{B43})$$

$$\begin{aligned} H_{5,3} &= H_{3,5}, H_{5,4} = H_{4,5}, H_{5,5} = -\frac{3}{2}\tilde{k}_1, H_{5,7} = \frac{3}{4}\tilde{k}_1, H_{5,8} = \frac{\sqrt{3}}{4}\tilde{k}_1; \\ H_{6,3} &= H_{3,6}, H_{6,4} = H_{4,6}, H_{6,6} = -\tilde{k}_2 - \frac{\tilde{k}_1}{2}, \end{aligned} \quad (\text{B44})$$

$$\begin{aligned} H_{6,7} &= \frac{\sqrt{3}}{4}\tilde{k}_1, H_{6,8} = \frac{\tilde{k}_1}{4}, H_{6,12} = \tilde{k}_2 e^{i[\mathbf{k} \cdot (-\mathbf{a}_{K1} + \mathbf{a}_{K2})]}; \\ H_{7,1} &= H_{1,7}^\dagger, H_{7,2} = H_{2,7}^\dagger, H_{7,5} = H_{5,7}, H_{7,6} = H_{6,7}, \end{aligned} \quad (\text{B45})$$

$$\begin{aligned} H_{7,7} &= -\frac{3}{4}\tilde{k}_2 - \frac{3}{4}\tilde{k}_1, H_{7,8} = \frac{\sqrt{3}}{4}\tilde{k}_2 - \frac{\sqrt{3}}{4}\tilde{k}_1; \\ H_{8,1} &= H_{1,8}^\dagger, H_{8,2} = H_{2,8}^\dagger, H_{8,5} = H_{5,8}, H_{8,6} = H_{6,8}, \end{aligned} \quad (\text{B46})$$

$$\begin{aligned} H_{8,7} &= H_{7,8}, H_{8,8} = -\frac{\tilde{k}_2}{4} - \frac{5}{4}\tilde{k}_1, H_{8,10} = \tilde{k}_1; \\ H_{9,3} &= H_{3,9}^\dagger, H_{9,4} = H_{4,9}^\dagger, H_{9,9} = -\frac{3}{4}k_2 - \frac{3}{4}k_1, \end{aligned} \quad (\text{B47})$$

$$\begin{aligned} H_{9,10} &= \frac{\sqrt{3}}{4}\tilde{k}_1 - \frac{\sqrt{3}}{4}\tilde{k}_2, H_{9,11} = \frac{3}{4}\tilde{k}_1, H_{9,12} = -\frac{\sqrt{3}}{4}\tilde{k}_1; \\ H_{10,3} &= H_{3,10}^\dagger, H_{10,4} = H_{4,10}^\dagger, H_{10,8} = H_{8,10}, H_{10,9} = H_{9,10}, \end{aligned} \quad (\text{B48})$$

$$\begin{aligned} H_{10,10} &= -\frac{\tilde{k}_2}{4} - \frac{5}{4}\tilde{k}_1, H_{10,11} = -\frac{\sqrt{3}}{4}\tilde{k}_1, H_{10,12} = \frac{\tilde{k}_1}{4}; \\ H_{11,1} &= H_{1,11}, H_{11,2} = H_{2,11}, H_{11,9} = H_{9,11}, \end{aligned} \quad (\text{B49})$$

$$\begin{aligned} H_{11,10} &= -\frac{\sqrt{3}}{4}\tilde{k}_1, H_{11,11} = -\frac{3}{2}\tilde{k}_1; \\ H_{12,1} &= H_{1,12}, H_{12,2} = H_{2,12}, H_{12,6} = H_{6,12}^\dagger, \end{aligned} \quad (\text{B50})$$

$$H_{12,9} = H_{9,12}, H_{12,10} = H_{10,12}, H_{12,12} = -\tilde{k}_2 - \frac{\tilde{k}_1}{2}, \quad (\text{B51})$$

where other elements are zero, and the mass matrix is

$$\text{Diag}(\mathbf{M}) = (m_1, m_1, m_2, m_2, m_1, m_1, m_2, m_2, m_1, m_1, m_2, m_2), \quad (\text{B52})$$

where other components are zero.

(4) The Lagrangian function of the C₃ unit cell [Fig. 10(i)] is

$$\begin{aligned} L = & \frac{1}{2}m_{1(p,q)}(P_M)[\ddot{u}_{1(p,q)}^2 + \dot{v}_{1(p,q)}^2] + \frac{1}{2}m_{2(p,q)}(P_M)[\ddot{u}_{2(p,q)}^2 + \dot{v}_{2(p,q)}^2] - \frac{1}{2}k_0\left[\frac{\sqrt{3}}{2}(u_1, v_1)_{(p,q)} - \frac{1}{2}(u_2, v_2)_{(p,q-1)}\right]^2 \\ & - \frac{1}{2}k_0\left[-\frac{\sqrt{3}}{2}(u_1, v_1)_{(p,q)} - \frac{1}{2}(u_2, v_2)_{(p+1,q-1)}\right]^2 - \frac{1}{2}k_0\left[\frac{\sqrt{3}}{2}(u_1, v_1)_{(p,q)} - \frac{1}{2}(u_2, v_2)_{(p,q+1)}\right]^2 \\ & - \frac{1}{2}k_0\left[-\frac{\sqrt{3}}{2}(u_1, v_1)_{(p,q)} - \frac{1}{2}(u_2, v_2)_{(p-1,q+1)}\right]^2 - \frac{1}{2}k_0[v_{1(p,q)} - v_{2(p,q)}]^2, \end{aligned} \quad (\text{B53})$$

where P_K = 0 indicates k₁ = k₂ = k₀. Based on the Lagrangian theory, we can obtain the following equations:

$$m_1(P_M)\ddot{u}_{1(0,0)}^2 = -k_0\left[\frac{3}{2}u_{1(0,0)} - \frac{3}{4}u_{2(0,-1)} - \frac{3}{4}u_{2(1,-1)} - \frac{\sqrt{3}}{4}v_{2(0,-1)} + \frac{\sqrt{3}}{4}v_{2(1,-1)}\right], \quad (\text{B54})$$

$$m_1(P_M)\ddot{v}_{1(0,0)}^2 = -k_0\left[-\frac{\sqrt{3}}{4}u_{2(0,-1)} + \frac{\sqrt{3}}{4}u_{2(1,-1)} + \frac{1}{2}v_{1(0,0)} - \frac{1}{4}v_{2(0,-1)} - \frac{1}{4}v_{2(1,-1)} - v_{1(0,0)} + v_{2(0,0)}\right], \quad (\text{B55})$$

$$m_2(P_M)\ddot{u}_{2(0,0)}^2 = -k_0\left[\frac{3}{2}u_{2(0,0)} - \frac{3}{4}u_{1(0,1)} - \frac{3}{4}u_{1(-1,1)} - \frac{\sqrt{3}}{4}v_{1(0,1)} + \frac{\sqrt{3}}{4}v_{1(-1,1)}\right], \quad (\text{B56})$$

$$m_2(P_M)\ddot{v}_{2(0,0)}^2 = -k_0\left[-\frac{\sqrt{3}}{4}u_{1(0,1)} + \frac{\sqrt{3}}{4}u_{1(-1,1)} + \frac{1}{2}v_{2(0,0)} - \frac{1}{4}v_{1(0,1)} - \frac{1}{4}v_{2(-1,1)} + v_{1(0,0)} - v_{2(0,0)}\right]. \quad (\text{B57})$$

Similarly, we can obtain

$$-m_1(P_M)\omega^2 u_{1(0,0)} = -\frac{3}{2}k_0 u_{1(0,0)} + \frac{3}{4}k_0 u_{2(0,0)} [e^{ik\cdot(-\mathbf{a}_2)} - e^{ik\cdot(\mathbf{a}_1+\mathbf{a}_2)}] - \frac{\sqrt{3}}{4}k_0 v_{2(0,0)} [e^{ik\cdot(-\mathbf{a}_2)} - e^{ik\cdot(\mathbf{a}_1-\mathbf{a}_2)}], \quad (\text{B58})$$

$$-m_1(P_M)\omega^2 v_{1(0,0)} = \frac{\sqrt{3}}{4}k_0 u_{2(0,0)} [e^{ik\cdot(-\mathbf{a}_2)} - e^{ik\cdot(\mathbf{a}_1-\mathbf{a}_2)}] - \frac{3}{2}k_0 v_{1(0,0)} + \frac{1}{4}k_0 u_{2(0,0)} [e^{ik\cdot(-\mathbf{a}_2)} + e^{ik\cdot(\mathbf{a}_1+\mathbf{a}_2)} + 1], \quad (\text{B59})$$

$$-m_2(P_M)\omega^2 u_{1(0,0)} = -\frac{3}{2}k_0 u_{2(0,0)} + \frac{3}{4}k_0 u_{1(0,0)} [e^{ik\cdot\mathbf{a}_2} + e^{ik\cdot(-\mathbf{a}_1+\mathbf{a}_2)}] + \frac{\sqrt{3}}{4}k_0 v_{1(0,0)} [e^{ik\cdot\mathbf{a}_2} - e^{ik\cdot(-\mathbf{a}_1+\mathbf{a}_2)}], \quad (\text{B60})$$

$$-m_2(P_M)\omega^2 v_{2(0,0)} = \frac{\sqrt{3}}{4}k_0 u_{1(0,0)} [e^{ik\cdot\mathbf{a}_2} - e^{ik\cdot(-\mathbf{a}_1+\mathbf{a}_2)}] - \frac{3}{2}k_0 v_{2(0,0)} + \frac{1}{4}k_0 v_{1(0,0)} [e^{ik\cdot\mathbf{a}_2} + e^{ik\cdot(-\mathbf{a}_1+\mathbf{a}_2)} + 1], \quad (\text{B61})$$

where $\mathbf{a}_{M1} = (\sqrt{3}a_0, 0)$ and $\mathbf{a}_{M2} = (\sqrt{3}/2a_0, 3/2a_0)$ are the crystal vectors, and the eigenequation is written as

$$[\mathbf{H}_{4\times 4} + \omega^2 \mathbf{M}_{4\times 4}(P_M)] \bar{\mathbf{u}}_{4\times 1} = \mathbf{0}, \quad (\text{B62})$$

where the elements of the Hamilton matrix are

$$\begin{aligned} \text{diag}(\mathbf{H}) &= -\frac{3}{2}k, H_{13} = \frac{3}{4}k [e^{-ik\cdot\mathbf{a}_{M2}} + e^{ik\cdot(\mathbf{a}_{M1}-\mathbf{a}_{M2})}], \\ H_{14} &= \frac{\sqrt{3}}{4}k [e^{ik\cdot(-\mathbf{a}_{M2})} - e^{ik\cdot(\mathbf{a}_{M1}-\mathbf{a}_{M2})}], \end{aligned} \quad (\text{B63})$$

$$\begin{aligned} H_{23} &= \frac{\sqrt{3}}{4}k [e^{-ik\cdot\mathbf{a}_{M2}} - e^{ik\cdot(\mathbf{a}_{M1}-\mathbf{a}_{M2})}], \\ H_{24} &= k \left[\frac{1}{4}e^{-ik\cdot\mathbf{a}_{M2}} + \frac{1}{4}e^{ik\cdot(\mathbf{a}_{M1}-\mathbf{a}_{M2})} + 1 \right], \end{aligned} \quad (\text{B64})$$

$$\begin{aligned} H_{31} &= \frac{3}{4}k [e^{ik\cdot\mathbf{a}_{M2}} + e^{ik\cdot(-\mathbf{a}_{M1}+\mathbf{a}_{M2})}], \\ H_{32} &= \frac{\sqrt{3}}{4}k [e^{ik\cdot\mathbf{a}_{M2}} - e^{ik\cdot(-\mathbf{a}_{M1}+\mathbf{a}_{M2})}], \end{aligned} \quad (\text{B65})$$

$$\begin{aligned} H_{41} &= \frac{\sqrt{3}}{4}k [e^{ik\cdot\mathbf{a}_{M2}} - e^{ik\cdot(-\mathbf{a}_{M1}+\mathbf{a}_{M2})}], \\ H_{42} &= k \left[\frac{1}{4}e^{ik\cdot\mathbf{a}_{M2}} + \frac{1}{4}e^{ik\cdot(-\mathbf{a}_{M1}+\mathbf{a}_{M2})} + 1 \right]. \end{aligned} \quad (\text{B66})$$

The active mass matrix is

$$\text{diag}(\mathbf{M}) = [m_1(P_M), m_1(P_M), m_2(P_M), m_2(P_M)], \quad (\text{B67})$$

where other components are zero.

REFERENCES

- ¹C. L. Kane and E. J. Mele, "Quantum spin Hall effect in graphene," *Phys. Rev. Lett.* **95**, 226801 (2005).

²B. A. Bernevig, T. L. Hughes, and S. C. Zhang, "Quantum spin Hall effect and topological phase transition in HgTe quantum wells," *Science* **314**, 1757–1761 (2006).

³M. König, S. Wiedmann, C. Brüne, A. Roth, H. Buhmann, L. W. Molenkamp, X. L. Qi, and S. C. Zhang, "Quantum spin Hall insulator state in HgTe quantum wells," *Science* **318**, 766–770 (2007).

⁴Z. X. Li, Y. S. Cao, and P. Yan, "Topological insulators and semimetals in classical magnetic systems," *Phys. Rep.* **915**, 1–64 (2021).

⁵L. Xin, Y. Siyuan, L. Harry, L. Minghui, and C. Yanfeng, "Topological mechanical metamaterials: A brief review," *Curr. Opin. Solid State Mater. Sci.* **24**, 100853 (2020).

⁶Y. Chen, X. N. Liu, and G. K. Hu, "Topological phase transition in mechanical honeycomb lattice," *J. Mech. Phys. Solids* **122**, 54–68 (2019).

⁷X. L. Qi and S. C. Zhang, "Topological insulators and superconductors," *Rev. Mod. Phys.* **83**, 1057 (2011).

⁸M. Z. Hasan and C. L. Kane, "Colloquium: Topological insulators," *Rev. Mod. Phys.* **82**, 3045 (2010).

⁹K. von Klitzing, T. Chakraborty, P. Kim, V. Madhavan, X. Dai, J. McIver, Y. Tokura, L. Savary, D. Smirnova, A. M. Rey, C. Felser, J. Gooth, and X. L. Qi, "40 years of the quantum Hall effect," *Nat. Rev. Phys.* **2**, 397–401 (2020).

¹⁰T. Vasileiadis, J. Varghese, V. Babacic, J. Gomis-Bresco, D. N. Urrios, and B. Graczykowski, "Progress and perspectives on phononic crystals," *J. Appl. Phys.* **129**, 160901 (2021).

¹¹G. C. Ma, M. Xiao, and C. T. Chan, "Topological phases in acoustic and mechanical systems," *Nat. Rev. Phys.* **1**, 281–294 (2019).

¹²H. B. Huang, J. J. Chen, and S. Y. Huo, "Recent advances in topological elastic metamaterials," *J. Phys.: Condens. Matter* **33**, 503002 (2021).

¹³W. A. Benalcazar, A. Bernevig, and T. L. Hughes, "Quantized electric multipole insulators," *Science* **357**, 61–66 (2017).

¹⁴F. D. M. Haldane, "Nobel lecture: Topological quantum matter," *Rev. Mod. Phys.* **89**, 040502 (2017).

¹⁵F. D. M. Haldane, "Model for a quantum Hall-effect without landau-levels-condensed-matter realization of the parity anomaly," *Phys. Rev. Lett.* **61**, 2015–2018 (1988).

¹⁶B. Y. Xie, H. X. Wang, X. J. Zhang, P. Zhan, J. H. Jiang, M. H. Lu, and Y. F. Chen, "Higher-order band topology," *Nat. Rev. Phys.* **3**, 520–532 (2021).

¹⁷B. Y. Xie, G. X. Su, H. W. Wang, F. Liu, L. Hu, S. Y. Yu, P. Zhan, M. H. Lu, Z. L. Wang, and Y. F. Chen, "Higher-order quantum spin Hall effect in a photonic crystal," *Nat. Commun.* **11**, 3768 (2020).

¹⁸M. Y. Kim, Z. B. Jacob, and J. Rho, "Recent advances in 2D, 3D and higher-order topological photonics," *Light Sci. Appl.* **9**, 130 (2020).

¹⁹T. Ozawa, H. M. Price, A. Amo, N. Goldman, M. Hafezi, L. Lu, M. C. Rechtsman, D. Schuster, J. Simon, O. Zilberberg, and I. Carusotto, "Topological photonics," *Rev. Mod. Phys.* **91**, 015006 (2019).

- ²⁰B. Y. Xie, H. F. Wang, H. X. Wang, X. Y. Zhu, J. H. Jiang, M. H. Lu, and Y. F. Chen, "Second-order photonic topological insulator with corner states," *Phys. Rev. B* **98**, 205147 (2018).
- ²¹X. J. Zhang, T. Zhang, M. H. Lu, and Y. F. Chen, "A review on non-Hermitian skin effect," *Adv. Phys.-X* **7**, 2109431 (2022).
- ²²B. L. Hu, Z. W. Zhang, H. X. Zhang, L. Y. Zheng, W. Xiong, Z. C. Yue, X. Y. Wang, J. Y. Xu, Y. Cheng, X. J. Liu, and J. Christensen, "Non-Hermitian topological whispering gallery," *Nature* **597**, 655–659 (2021).
- ²³L. Xiao, T. S. Deng, K. K. Wang, G. Y. Zhu, Z. Wang, W. Yi, and P. Xue, "Non-Hermitian bulk-boundary correspondence in quantum dynamics," *Nat. Phys.* **16**, 761–766 (2020).
- ²⁴Y. Ashida, Z. P. Gong, and M. Ueda, "Non-Hermitian physics," *Adv. Phys.* **69**, 249–435 (2020).
- ²⁵S. Y. Yao and Z. Wang, "Edge states and topological invariants of non-Hermitian systems," *Phys. Rev. Lett.* **121**, 086803 (2018).
- ²⁶S. Y. Yao, F. Song, and Z. Wang, "Non-Hermitian Chern bands," *Phys. Rev. Lett.* **121**, 136802 (2018).
- ²⁷G. Q. Xu, Y. H. Yang, X. Zhou, H. S. Chen, A. Alu, and C. W. Qiu, "Diffusive topological transport in spatiotemporal thermal lattices," *Nat. Phys.* **18**, 450–456 (2022).
- ²⁸K. Hofhuis, S. H. Skjaervo, S. Parchenko, H. Arava, Z. C. Luo, A. Kleibert, P. M. Derlet, and L. J. Heyderman, "Real-space imaging of phase transitions in bridged artificial kagome spin ice," *Nat. Phys.* **18**, 699–705 (2022).
- ²⁹Y. T. Yang, J. Y. Lu, M. Yan, X. Q. Huang, W. Y. Deng, and Z. Y. Liu, "Hybrid-order topological insulators in a phononic crystal," *Phys. Rev. Lett.* **126**, 156801 (2021).
- ³⁰G. Q. Xu, Y. Li, W. Li, S. H. Fan, and C. W. Qiu, "Configurable phase transitions in a topological thermal material," *Phys. Rev. Lett.* **127**, 105901 (2021).
- ³¹N. P. Mitchell, A. M. Turner, and W. T. M. Irvine, "Real-space origin of topological band gaps, localization, and reentrant phase transitions in gyroscopic metamaterials," *Phys. Rev. E* **104**, 025007 (2021).
- ³²S. Guddala, F. Komissarenko, S. Kiriushechkina, A. Vakulenko, M. Li, V. M. Menon, A. Alù, and A. B. Khanikaev, "Topological phonon-polariton funneling in midinfrared metasurfaces," *Science* **374**, 225–227 (2021).
- ³³Y. F. Zhang, B. Li, Q. S. Zheng, G. M. Genin, and C. Q. Chen, "Programmable and robust static topological solitons in mechanical metamaterials," *Nat. Commun.* **10**, 5605 (2019).
- ³⁴A. Souslov, B. C. van-Zuiden, D. Bartolo, and V. Vitelli, "Topological sound in active-liquid metamaterials," *Nat. Phys.* **13**, 1091–1094 (2017).
- ³⁵M. Kiczynski, S. K. Gorman, H. Geng, M. B. Donnelly, Y. Chung, Y. He, J. G. Keizer, and M. Y. Simmons, "Engineering topological states in atom-based semiconductor quantum dots," *Nature* **606**, 694–699 (2022).
- ³⁶H. Y. Fan, B. Z. Xia, L. Tong, S. J. Zheng, and D. J. Yu, "Elastic higher-order topological insulator with topologically protected corner states," *Phys. Rev. Lett.* **122**, 204301 (2019).
- ³⁷S. N. Kempkes, M. R. Slot, J. J. van-den-Broeke, P. Capiod, W. A. Benalcazar, D. Vanmaekelbergh, D. Berciou, I. Swart, and C. Morais Smith, "Robust zero-energy modes in an electronic higher-order topological insulator," *Nat. Mater.* **18**, 1292–1297 (2019).
- ³⁸X. Ni, M. Weiner, A. Alù, and A. B. Khanikaev, "Observation of higher-order topological acoustic states protected by generalized chiral symmetry," *Nat. Mater.* **18**, 113–120 (2019).
- ³⁹H. R. Xue, Y. H. Yang, F. Gao, Y. D. Chong, and B. L. Zhang, "Acoustic higher-order topological insulator on a kagome lattice," *Nat. Mater.* **18**, 108–112 (2019).
- ⁴⁰X. J. Zhang, H. X. Wang, Z. K. Lin, Y. Tian, B. Xie, M. H. Lu, Y. F. Chen, and J. H. Jiang, "Second-order topology and multidimensional topological transitions in sonic crystals," *Nat. Phys.* **15**, 582–588 (2019).
- ⁴¹C. He, H. S. Lai, B. He, S. Y. Yu, X. Y. Xu, M. H. Lu, and Y. F. Chen, "Acoustic analogues of three-dimensional topological insulators," *Nat. Commun.* **11**, 2318 (2020).
- ⁴²X. Ni, M. Y. Li, M. Weiner, A. Alu, and A. B. Khanikaev, "Demonstration of a quantized acoustic octupole topological insulator," *Nat. Commun.* **11**, 2108 (2020).
- ⁴³M. Weiner, X. Ni, M. Y. Li, A. Alu, and A. B. Khanikaev, "Demonstration of a third-order hierarchy of topological states in a three-dimensional acoustic metamaterial," *Sci. Adv.* **6**, eaay4166 (2020).
- ⁴⁴Z. Xiong, Z. K. Lin, H. X. Wang, X. J. Zhang, M. H. Lu, Y. F. Chen, and J. H. Jiang, "Corner states and topological transitions in two-dimensional higher-order topological sonic crystals with inversion symmetry," *Phys. Rev. B* **102**, 125144 (2020).
- ⁴⁵Z. Yang, X. Li, Y. Y. Peng, X. Y. Zou, and J. C. Cheng, "Helical higher-order topological states in an acoustic crystalline insulator," *Phys. Rev. Lett.* **125**, 255502 (2020).
- ⁴⁶J. Kosata and O. Zilberberg, "Second-order topological modes in two-dimensional continuous media," *Phys. Rev. Res.* **3**, L032029 (2021).
- ⁴⁷H. H. Qiu, M. Xiao, F. Zhang, and C. Y. Qiu, "Higher-order Dirac sonic crystals," *Phys. Rev. Lett.* **127**, 146601 (2021).
- ⁴⁸A. Vakulenko, S. Kiriushechkina, M. S. Wang, M. Y. Li, D. Zhirihi, X. Ni, S. Guddala, D. Korobkin, A. Alù, and A. B. Khanikaev, "Near-field characterization of higher-order topological photonic states at optical frequencies," *Adv. Sci.* **33**, 2004376 (2021).
- ⁴⁹Q. Wei, X. W. Zhang, W. Y. Deng, J. Y. Lu, X. Q. Huang, M. Yan, G. Chen, Z. Y. Liu, and S. T. Jia, "Higher-order topological semimetal in acoustic crystals," *Nat. Mater.* **20**, 812–817 (2021).
- ⁵⁰C. Q. Xu, Z. G. Chen, G. Q. Zhang, G. C. Ma, and Y. Wu, "Multi-dimensional wave steering with higher-order topological phononic crystal," *Sci. Bull.* **66**, 1740–1745 (2021).
- ⁵¹M. A. Miri and A. Alu, "Exceptional points in optics and photonics," *Science* **363**, eaar7709 (2019).
- ⁵²S. K. Ozdemir, S. Rotter, F. Nori, and L. Yang, "Parity-time symmetry and exceptional points in photonics," *Nat. Mater.* **18**, 783–798 (2019).
- ⁵³K. Sone, Y. Ashida, and T. Sagawa, "Exceptional non-Hermitian topological edge mode and its application to active matter," *Nat. Commun.* **11**, 5745 (2020).
- ⁵⁴E. J. Bergholtz, J. C. Budich, and F. K. Kunst, "Exceptional topology of non-Hermitian systems," *Rev. Mod. Phys.* **93**, 015005 (2021).
- ⁵⁵M. M. Denner, A. Skurativska, F. Schindler, M. H. Fischer, R. Thomale, T. Bzdusek, and T. Neupert, "Exceptional topological insulators," *Nat. Commun.* **12**, 5681 (2021).
- ⁵⁶K. Wang, A. Dutt, C. C. Wojcik, and S. H. Fan, "Topological complex-energy braiding of non-Hermitian bands," *Nature* **598**, 59–64 (2021).
- ⁵⁷R. Huang, S. K. Ozdemir, J. Q. Liao, F. Minganti, L. M. Kuang, F. Nori, and H. Jing, "Exceptional photon blockade: Engineering photon blockade with chiral exceptional points," *Laser Photonics Rev.* **16**, 2100430 (2022).
- ⁵⁸L. Zhang, Y. H. Yang, Y. Ge, Y. J. Guan, Q. L. Chen, Q. H. Yan, F. J. Chen, R. Xi, Y. Z. Li, D. Jia, S. Q. Yuan, H. X. Sun, H. S. Chen, and B. L. Zhang, "Acoustic non-Hermitian skin effect from twisted winding topology," *Nat. Commun.* **12**, 6297 (2021). doi:10.1038/s41467-021-26619-8
- ⁵⁹Z. W. Zhang, Q. Wei, Y. Cheng, T. Zhang, D. J. Wu, and X. J. Liu, "Topological creation of acoustic pseudospin multipoles in a flow-free symmetry-broken metamaterial lattice," *Phys. Rev. Lett.* **118**, 084303 (2017).
- ⁶⁰M. Y. Li, D. Zhirihi, M. Gorlach, X. Ni, D. Filonov, A. Slobozhanyuk, A. Alu, and A. B. Khanikaev, "Higher-order topological states in photonic kagome crystals with long-range interactions," *Nat. Photonics* **14**, 89–94 (2020).
- ⁶¹J. W. Dong, X. D. Chen, H. Y. Zhu, Y. Wang, and X. Zhang, "Valley photonic crystals for control of spin and topology," *Nat. Mater.* **16**, 298–302 (2017).
- ⁶²J. Vila, R. K. Pal, and M. Ruzzene, "Observation of topological valley modes in an elastic hexagonal lattice," *Phys. Rev. B* **96**, 134307 (2017).
- ⁶³X. Ni, D. Purtseladze, D. A. Smirnova, A. Slobozhanyuk, A. Alu, and A. B. Khanikaev, "Spin- and valley-polarized one-way Klein tunneling in photonic topological insulators," *Sci. Adv.* **4**, eaap8802 (2018).
- ⁶⁴A. Drouot and M. I. Weinstein, "Edge states and the valley Hall effect," *Adv. Math.* **368**, 107142 (2020).

- ⁶⁵Z. H. Tian, C. Shen, J. F. Li, E. Reit, H. Bachman, J. E. S. Socolar, S. A. Cummer, and T. J. Huang, “Dispersion tuning and route reconfiguration of acoustic waves in valley topological phononic crystals,” *Nat. Commun.* **11**, 762 (2020).
- ⁶⁶Y. Wu, R. Chaunsali, H. Yasuda, K. P. Yu, and J. Yang, “Dial-in topological metamaterials based on bistable Stewart platform,” *Sci. Rep.* **10**, 112 (2020).
- ⁶⁷Z. X. Xu, X. H. Kong, R. J. Davis, D. Bisharat, Y. Zhou, X. X. Yin, and D. F. Sievenpiper, “Topological valley transport under long-range deformations,” *Phys. Rev. Res.* **2**, 013209 (2020).
- ⁶⁸Q. Zhang, Y. Chen, K. Zhang, and G. K. Hu, “Dirac degeneracy and elastic topological valley modes induced by local resonant states,” *Phys. Rev. B* **101**, 014101 (2020).
- ⁶⁹S. Y. Huo, J. J. Chen, H. B. Huang, Y. J. Wei, Z. H. Tan, L. Y. Feng, and X. P. Xie, “Experimental demonstration of valley-protected backscattering suppression and interlayer topological transport for elastic wave in three-dimensional phononic crystals,” *Mech. Syst. Signal Process.* **154**, 107543 (2021).
- ⁷⁰Z. H. Lan, J. W. You, Q. Ren, W. E. I. Sha, and N. C. Panoiu, “Second-harmonic generation via double topological valley-Hall kink modes in all-dielectric photonic crystals,” *Phys. Rev. A* **103**, L041502 (2021).
- ⁷¹J. W. Ma, X. Xi, and X. K. Sun, “Experimental demonstration of dual-band nano-electromechanical valley-Hall topological metamaterials,” *Adv. Mater.* **33**, 2006521 (2021).
- ⁷²H. R. Xue, Y. H. Yang, and B. L. Zhang, “Topological valley photonics: Physics and device applications,” *Adv. Photonics Res.* **2**, 2100013 (2021).
- ⁷³F. Gao, H. R. Xue, Z. J. Yang, K. F. Lai, Y. Yu, X. Lin, Y. D. Chong, G. Shvets, and B. L. Zhang, “Topologically protected refraction of robust kink states in valley photonic crystals,” *Nat. Phys.* **14**, 140–144 (2018).
- ⁷⁴J. Y. Lu, C. Y. Qiu, W. Y. Deng, X. Q. Huang, F. Li, F. Zhang, S. Q. Chen, and Z. Y. Liu, “Valley topological phases in bilayer sonic crystals,” *Phys. Rev. Lett.* **120**, 116802 (2018).
- ⁷⁵X. X. Wu, Z. Y. Li, J. Chen, X. Li, J. X. Tian, Y. Z. Huang, S. X. Wang, W. X. Lu, B. Hou, C. T. Chan, and W. J. Wen, “Interlayer topological transport and devices based on layer pseudospins in photonic valley-Hall phases,” *Adv. Opt. Mater.* **7**, 1900872 (2019).
- ⁷⁶X. Z. Han, L. Li, Y. J. Hu, L. Ling, Z. G. Geng, Y. G. Peng, D. G. Zhao, X. F. Zhu, and X. L. Wang, “Valley like edge states in chiral phononic crystals with Dirac degeneracies beyond high-symmetry points and boundaries of Brillouin zones,” *Phys. Rev. Appl.* **14**, 024091 (2020).
- ⁷⁷N. Gao, S. C. Qu, L. Si, J. Wang, and W. Q. Chen, “Broadband topological valley transport of elastic wave in reconfigurable phononic crystal plate,” *Appl. Phys. Lett.* **118**, 063502 (2021).
- ⁷⁸W. T. Yuan, J. F. Zhao, Y. Long, J. Ren, and Z. Zhong, “Multi-branch valley-chiral edge states of antisymmetric plate wave in phononic crystal plates with double-sided symmetric pillars,” *Int. J. Mech. Sci.* **197**, 106347 (2021).
- ⁷⁹W. B. Fang, C. Y. Han, Y. Y. Chen, and Y. J. Liu, “Valley Hall elastic edge states in locally resonant metamaterials,” *Materials* **15**, 1491 (2022).
- ⁸⁰S. Q. Wu, Z.-K. Lin, B. Jiang, X. X. Zhou, H. Bo, and J. H. Jiang, “Observation of higher-order topological states in acoustic twisted moiré superlattice,” *Phys. Rev. Appl.* **17**, 034061 (2022).
- ⁸¹C. He, S. Y. Yu, H. Ge, H. Q. Wang, Y. Tian, H. J. Zhang, X. C. Sun, Y. B. Chen, J. Zhou, M. H. Lu, and Y. F. Chen, “Three-dimensional topological acoustic crystals with pseudospin-valley coupled saddle surface states,” *Nat. Commun.* **9**, 4555 (2018).
- ⁸²X. J. Tan, S. Chen, B. Wang, J. Tang, L. C. Wang, S. W. Zhu, K. L. Yao, and P. F. Xu, “Real-time tunable negative stiffness mechanical metamaterial,” *Extreme Mech. Lett.* **41**, 100990 (2020).
- ⁸³Y. Zhou, P. R. Bandaru, and D. F. Sievenpiper, “Quantum-spin-Hall topological insulator in a spring-mass system,” *New J. Phys.* **20**, 123011 (2018).
- ⁸⁴H. Chen, H. Nassar, and G. L. Huang, “A study of topological effects in 1D and 2D mechanical lattices,” *J. Mech. Phys. Solids* **117**, 22–36 (2018).
- ⁸⁵R. K. Pal and M. Ruzzene, “Edge waves in plates with resonators: An elastic analogue of the quantum valley Hall effect,” *New J. Phys.* **19**, 025001 (2017).
- ⁸⁶H. W. Dong, S. D. Zhao, R. Zhu, Y. S. Wang, L. Cheng, and C. Z. Zhang, “Customizing acoustic Dirac cones and topological insulators in square lattices by topology optimization,” *J. Sound Vib.* **493**, 115687 (2021).
- ⁸⁷Y. F. Chen, F. Meng, and X. D. Huang, “Creating acoustic topological insulators through topology optimization,” *Mech. Syst. Signal Process.* **146**, 107054 (2021).
- ⁸⁸H. K. Zhang, Z. Kang, Y. Q. Wang, and W. J. Wu, “Isotropic “quasi-fluid” metamaterials designed by topology optimization,” *Adv. Theory Simul.* **3**, 1900182 (2020).
- ⁸⁹Z. L. Du, H. Chen, and G. L. Huang, “Optimal quantum valley Hall insulators by rational engineering Berry curvature and band structure,” *J. Mech. Phys. Solids* **135**, 103784 (2020).
- ⁹⁰S. S. Nanthakumar, X. Y. Zhuang, H. S. Park, C. Nguyen, Y. Y. Chen, and T. Rabczuk, “Inverse design of quantum spin Hall-based phononic topological insulators,” *J. Mech. Phys. Solids* **125**, 550–571 (2019).
- ⁹¹R. E. Christiansen, F. W. Wang, and O. Sigmund, “Topological insulators by topology optimization,” *Phys. Rev. Lett.* **122**, 234502 (2019).
- ⁹²C. Shang, S. Liu, R. W. Shao, P. Han, X. N. Zang, X. L. Zhang, K. N. Salama, W. L. Gao, C. H. Lee, R. Thomale, A. Manchon, S. Zhang, T. J. Cui, and U. Schwingenschlögl, “Experimental identification of the second-order non-Hermitian skin effect with physics-graph-informed machine learning,” *Adv. Sci.* **9**, 2020922 (2022).
- ⁹³W. Ma, Z. C. Liu, Z. A. Kudyshev, A. Boltasseva, W. S. Cai, and Y. M. Liu, “Deep learning for the design of photonic structures,” *Nat. Photonics* **15**, 77–90 (2021).
- ⁹⁴H. Araki, T. Mizoguchi, and Y. Hatsugai, “Phase diagram of a disordered higher-order topological insulator: A machine learning study,” *Phys. Rev. B* **99**, 085406 (2019).
- ⁹⁵W. Ma, F. Cheng, and Y. M. Liu, “Deep-learning-enabled on-demand design of chiral metamaterials,” *ACS Nano* **12**, 6326–6334 (2018).
- ⁹⁶M. Oudich, N. J. Gerard, Y. C. Deng, and Y. Jing, “Bandgap engineering in phononic crystals and elastic metamaterials,” *arXiv:2207.05234* (2022).
- ⁹⁷M. Akamatsu, R. Vasan, D. Serwas, M. A. Ferrin, P. Rangamani, and D. G. Rubin, “Principles of self-organization and load adaptation by the actin cytoskeleton during clathrin-mediated endocytosis,” *Elife* **9**, e49840 (2021).
- ⁹⁸V. Venturini, F. Pezzano, F. Català Castro, H. M. Häkkinen, S. Jiménez-Delgado, M. Colomer-Rosell, M. Marro, Q. Tolosa-Ramon, S. Paz-López, M. A. Valverde, J. Weghuber, P. Loza-Alvarez, M. Krieg, S. Wieser, and V. Ruprecht, “The nucleus measures shape changes for cellular proprioception to control dynamic cell behavior,” *Science* **370**, eaba2644 (2020).
- ⁹⁹A. J. Lomakin, C. J. Cattin, D. Cuvelier, Z. Alraies, M. Molina, G. P. F. Nader, N. Srivastava, P. J. Saez, J. M. Garcia-Arcos, I. Y. Zhitnyak, A. Bhargava, M. K. Driscoll, E. S. Welf, R. Fiolka, R. J. Petrie, N. S. De Silva, J. M. Gonzalez-Granado, N. Manel, A. M. Lennon-Dumenil, D. J. Muller, and M. Piel, “The nucleus acts as a ruler tailoring cell responses to spatial constraints,” *Science* **370**, eaba2894 (2020).
- ¹⁰⁰J. Teyssier, S. V. Saenko, D. van der Marel, and M. C. Milinkovitch, “Photonic crystals cause active colour change in chameleons,” *Nat. Commun.* **6**, 6368 (2015).
- ¹⁰¹Y. J. Zhao, Z. Y. Xie, H. C. Gu, C. Zhu, and Z. Z. Gu, “Bio-inspired variable structural color materials,” *Chem. Soc. Rev.* **41**, 3297–3317 (2012).
- ¹⁰²J. P. Vigneron, J. M. Pasteels, D. M. Windsor, Z. Vertes, M. Rassart, T. Seldrum, J. Dumont, O. Deparis, V. Lousse, L. P. Biro, D. Ertz, and V. Welch, “Switchable reflector in the Panamanian tortoise beetle *Charidotella egregia* (Chrysomelidae: Cassidinae),” *Phys. Rev. E* **76**, 031907 (2007).
- ¹⁰³S. C. Li, M. M. Lerch, J. T. Waters, B. L. Deng, R. S. Martens, Y. X. Yao, D. Y. Kim, K. Bertoldi, A. Grinthal, A. C. Balazs, and J. Aizenberg, “Self-regulated non-reciprocal motions in single-material microstructures,” *Nature* **605**, 76–83 (2022).
- ¹⁰⁴Z. J. Wang, K. Li, Q. G. He, and S. Q. Cai, “A light-powered ultralight tensegrity robot with high deformability and load capacity,” *Adv. Mater.* **31**, 1806849 (2019).
- ¹⁰⁵S. J. Park, M. Gazzola, K. S. Park, S. Park, V. Di Santo, E. L. Blevins, J. U. Lind, P. H. Campbell, S. Dauth, A. K. Capulli, F. S. Pasqualini, S. Ahn,

- A. Cho, H. Y. Yuan, B. M. Maoz, R. Vijaykumar, J. W. Choi, K. Deisseroth, G. V. Lauder, L. Mahadevan, and K. K. Parker, "Phototactic guidance of a tissue-engineered soft-robotic ray," *Science* **353**, 158–162 (2016).
- ¹⁰⁶Q. J. Ze, S. Wu, J. Nishikawa, J. Z. Dai, Y. Sun, S. Leanza, C. Zemelka, L. S. Novelino, G. H. Paulino, and R. R. Zhao, "Soft robotic origami crawler," *Sci. Adv.* **8**, eabm7834 (2022).
- ¹⁰⁷W. D. Wang, G. Gardi, P. Malgaretti, V. Kishore, L. Koens, D. Son, H. Gilbert, Z. Y. Wu, P. Harwani, E. Lauga, C. Holm, and M. Sitti, "Order and information in the patterns of spinning magnetic micro-disks at the air-water interface," *Sci. Adv.* **8**, eabk0685 (2022).
- ¹⁰⁸S. M. Montgomery, S. Wu, X. Kuang, C. D. Armstrong, C. Zemelka, Q. J. Ze, R. D. Zhang, R. K. Zhao, and H. J. Qi, "Magneto-mechanical metamaterials with widely tunable mechanical properties and acoustic bandgaps," *Adv. Funct. Mater.* **31**, 2005319 (2021).
- ¹⁰⁹H. Lee, Y. Jang, J. K. Choe, S. Lee, H. Song, J. P. Lee, N. Lone, and J. Kim, "3D-printed programmable tensegrity for soft robotics," *Sci. Rob.* **5**, eaay9024 (2020).
- ¹¹⁰S. Wu, Q. J. Ze, R. D. Zhang, N. Hu, Y. Cheng, F. Y. Yang, and R. K. Zhao, "Symmetry-breaking actuation mechanism for soft robotics and active metamaterials," *ACS Appl. Mater. Interfaces* **11**, 41649–41658 (2019).
- ¹¹¹H. R. Gu, Q. Boehler, D. Ahmed, and B. J. Nelson, "Magnetic quadrupole assemblies with arbitrary shapes and magnetizations," *Sci. Rob.* **4**, eaax8977 (2019).
- ¹¹²G. R. Li, X. P. Chen, F. H. Zhou, Y. M. Liang, Y. H. Xiao, X. Cao, Z. Zhang, M. Q. Zhang, B. S. Wu, S. Y. Yin, Y. Xu, H. B. Fan, Z. Chen, W. Song, W. J. Yang, B. B. Pan, J. Y. Hou, W. F. Zou, S. P. He, X. X. Yang, G. Y. Mao, Z. Jia, H. F. Zhou, T. F. Li, S. X. Qu, Z. B. Xu, Z. L. Huang, Y. W. Luo, T. Xie, J. Gu, S. Q. Zhu, and W. Yang, "Self-powered soft robot in the Mariana Trench," *Nature* **591**, 66–71 (2021).
- ¹¹³v. Acome, S. K. Mitchell, T. G. Morrissey, M. B. Emmett, C. Benjamins, M. King, M. Radakovitz, and C. Keplinger, "Hydraulically amplified self-healing electrostatic actuators with muscle-like performance," *Science* **359**, 61–65 (2018).
- ¹¹⁴H. C. Cui, D. S. Yao, R. Hensleigh, H. T. Lu, A. Calderon, Z. P. Xu, S. Davaria, Z. Wang, P. Mercier, P. Tarazaga, and X. Y. R. Zheng, "Design and printing of proprioceptive three-dimensional architected robotic metamaterials," *Science* **376**, 1287–1293 (2022).
- ¹¹⁵A. E. Forte, P. Z. Hanakata, L. S. Jin, E. Zari, A. Zareei, M. C. Fernandes, L. Sumner, J. Alvarez, and K. Bertoldi, "Inverse design of inflatable soft membranes through machine learning," *Adv. Funct. Mater.* **32**, 2111610 (2022).
- ¹¹⁶N. Vasios, B. L. Deng, B. Gorissen, and K. Bertoldi, "Universally bistable shells with nonzero Gaussian curvature for two-way transition waves," *Nat. Commun.* **12**, 695 (2021).
- ¹¹⁷D. Melancon, B. Gorissen, C. J. García-Mora, C. Hoberman, and K. Bertoldi, "Multistable inflatable origami structures at the metre scale," *Nature* **592**, 545–550 (2021).
- ¹¹⁸T. J. Jones, E. Jambon-Puillet, J. Marthelot, and P. T. Brun, "Bubble casting soft robotics," *Nature* **599**, 229–233 (2021).
- ¹¹⁹H. Jiang, Z. C. Wang, Y. S. Jin, X. T. Chen, P. J. Li, Y. H. Gan, S. Lin, and X. P. Chen, "Hierarchical control of soft manipulators towards unstructured interactions," *Int. J. Rob. Res.* **40**, 411–434 (2021).
- ¹²⁰C. H. Feng, Q. Li, Y. J. Zeng, X. Su, and H. B. Yu, "2D to 3D convertible terahertz chiral metamaterial with integrated pneumatic actuator," *Opt. Express* **26**, 14421–14432 (2018).
- ¹²¹C. L. Feng, F. Shi, J. Shao, Q. Li, and H. B. Yu, "Pneumatically actuated tunable terahertz metamaterial absorber with dual-side tuning capability," *IEEE Photonics J.* **9**, 4600409 (2017).
- ¹²²D. Yang, B. Mosadegh, A. Ainla, B. Lee, F. Khashai, Z. G. Suo, K. Bertoldi, and G. M. Whitesides, "Buckling of elastomeric beams enables actuation of soft machines," *Adv. Mater.* **27**, 6323–6327 (2015).
- ¹²³B. Mosadegh, P. Polygerinos, C. Keplinger, S. Wennstedt, R. F. Shepherd, U. Gupta, J. Shim, K. Bertoldi, C. J. Walsh, and G. M. Whitesides, "Pneumatic networks for soft robotics that actuate rapidly," *Adv. Funct. Mater.* **24**, 2163–2170 (2014).
- ¹²⁴J. Z. Gu, Y. Y. Lin, Q. Cui, X. Q. Li, J. J. Li, L. Y. Sun, C. Yao, F. T. Ying, G. Y. Wang, and L. N. Yao, "PneuMesh: Pneumatic-driven truss-based shape changing system," in *CHI Conference on Human Factors in Computing Systems* (Association for Computing Machinery, 2022), pp. 1–12.
- ¹²⁵J. B. Nielsen, R. L. Hanson, H. M. Almughamsi, C. Pang, T. R. Fish, and A. T. Woolley, "Microfluidics: Innovations in materials and their fabrication and functionalization," *Anal. Chem.* **92**, 150–168 (2020).
- ¹²⁶Q. D. Zhang, M. Zhang, L. Djeghlaf, J. Bataille, J. Gamby, A. M. Haghiri-Gosnet, and A. Pallandre, "Logic digital fluidic in miniaturized functional devices: Perspective to the next generation of microfluidic lab-on-chips," *Electrophoresis* **38**, 953–976 (2017).
- ¹²⁷J. Kim, A. M. Stockton, E. C. Jensen, and R. A. Mathies, "Pneumatically actuated microvalve circuits for programmable automation of chemical and biochemical analysis," *Lab. Chip* **16**, 812–819 (2016).
- ¹²⁸B. Mosadegh, A. D. Mazzeo, R. F. Shepherd, S. A. Morin, U. Gupta, I. Z. Sani, D. Lai, S. Takayama, and G. M. Whitesides, "Control of soft machines using actuators operated by a Braille display," *Lab. Chip* **14**, 189–199 (2014).
- ¹²⁹M. Han, X. Guo, X. Chen, C. Liang, H. Zhao, Q. Zhang, W. Bai, F. Zhang, H. Wei, C. Wu, Q. Cui, S. Yao, B. Sun, Y. Yang, Q. Yang, Y. Ma, Z. Xue, J. W. Kwak, T. Jin, Q. Tu, E. Song, Z. Tian, Y. Mei, D. Fang, H. Zhang, Y. Huang, Y. Zhang, and J. A. Rogers, "Submillimeter scale multimaterial terrestrial robots," *Sci. Rob.* **7**, eabn0602 (2022).
- ¹³⁰J. Liao, C. Ye, J. Guo, C. E. Garciamendez-Mijares, P. Agrawal, X. Kuang, J. O. Japo, Z. Wang, X. Mu, W. Li, T. Ching, L. S. Mille, C. Zhu, X. Zhang, Z. Z. Gu, and Y. S. Zhang, "3D-printable colloidal photonic crystals," *Mater. Today* **56**, 29–41 (2022).
- ¹³¹X. G. Guo, X. Y. Ni, J. H. Li, H. Zhang, F. Zhang, H. B. Yu, J. Wu, Y. Bai, H. S. Lei, Y. G. Huang, J. A. Rogers, and Y. H. Zhang, "Designing mechanical metamaterials with kirigami-inspired, hierarchical constructions for giant positive and negative thermal expansion," *Adv. Mater.* **33**, 2004919 (2021).
- ¹³²R. Tao, L. Xi, W. W. Wu, Y. Li, B. B. Liao, L. W. Liu, J. S. Leng, and D. N. Fang, "4D printed multi-stable metamaterials with mechanically tunable performance," *Compos. Struct.* **252**, 112663 (2020).
- ¹³³H. K. Zhang and X. Q. Feng, "Buckling-regulated bandgaps of soft metamaterials with chiral hierarchical microstructure," *Extreme Mech. Lett.* **43**, 101166 (2021).
- ¹³⁴H. Luan, Q. Zhang, T. L. Liu, X. Wang, S. Zhao, H. Wang, S. Yao, Y. Xue, J. W. Kwak, W. Bai, Y. Xu, M. Han, K. Li, Z. Li, X. Ni, J. Ye, D. Choi, Q. Yang, J. H. Kim, S. Li, S. Chen, C. Wu, D. Lu, J. K. Chang, Z. Xie, Y. Huang, and J. A. Rogers, "Complex 3D microfluidic architectures formed by mechanically guided compressive buckling," *Sci. Adv.* **7**, eabj3686 (2021).
- ¹³⁵S. Li, B. Deng, A. Grinthal, A. Schneider-Yamamura, J. Kang, R. S. Martens, C. T. Zhang, J. Li, S. Yu, K. Bertoldi, and J. Aizenberg, "Liquid-induced topological transformations of cellular microstructures," *Nature* **592**, 386–391 (2021).
- ¹³⁶Y. L. Wei, Q. S. Yang, L. H. Ma, R. Tao, and J. J. Shang, "Design and analysis of 2D/3D negative hydration expansion metamaterial driven by hydrogel," *Mater. Des.* **196**, 109084 (2020).
- ¹³⁷S. Kriegman, D. Blackiston, M. Levin, and J. Bongard, "A scalable pipeline for designing reconfigurable organisms," *Proc. Natl. Acad. Sci. U.S.A.* **117**, 1853–1859 (2020).
- ¹³⁸Z. W. Li, Y. Seo, O. Aydin, M. Elhebeary, R. D. Kamm, H. Kong, and M. T. A. Saif, "Biohybrid valveless pump-bot powered by engineered skeletal muscle," *Proc. Natl. Acad. Sci. U.S.A.* **116**, 1543–1548 (2019).
- ¹³⁹Z. Y. Chen, F. F. Fu, Y. R. Yu, H. Wang, Y. X. Shang, and Y. J. Zhao, "Cardiomyocytes-actuated morpho butterfly wings," *Adv. Mater.* **31**, 1805431 (2019).
- ¹⁴⁰Y. Morimoto, H. Onoe, and S. Takeuchi, "Biohybrid robot powered by an antagonistic pair of skeletal muscle tissues," *Sci. Rob.* **3**, eaat4440 (2018).
- ¹⁴¹F. F. Fu, L. R. Shang, Z. Y. Chen, Y. R. Yu, and Y. J. Zhao, "Bioinspired living structural color hydrogels," *Sci. Rob.* **3**, eaar8580 (2018).

- ¹⁴²L. Ricotti, B. Trimmer, A. W. Feinberg, R. Raman, K. K. Parker, R. Bashir, M. Sitti, S. Martel, P. Dario, and A. Menciassi, "Biohybrid actuators for robotics: A review of devices actuated by living cells," *Sci. Rob.* **2**, eaaoq495 (2017).
- ¹⁴³J. U. Lind, T. A. Busbee, A. D. Valentine, F. S. Pasqualini, H. Y. Yuan, M. Yadid, S. J. Park, A. Kotikian, A. P. Nesmith, P. H. Campbell, J. J. Vlassak, J. A. Lewis, and K. K. Parker, "Instrumented cardiac microphysiological devices via multimaterial three-dimensional printing," *Nat. Mater.* **16**, 303–308 (2017).
- ¹⁴⁴J. Liu, T. Y. Gu, S. C. Shan, S. H. Kang, J. C. Weaver, and K. Bertoldi, "Harnessing buckling to design architected materials that exhibit effective negative swelling," *Adv. Mater.* **28**, 6619–6624 (2016).
- ¹⁴⁵J. C. Nawroth, H. Lee, A. W. Feinberg, C. M. Ripplinger, M. L. McCain, A. Grosberg, J. O. Dabiri, and K. K. Parker, "A tissue-engineered jellyfish with biomimetic propulsion," *Nat. Biotechnol.* **30**, 792–797 (2012).
- ¹⁴⁶B. Pokroy, S. H. Kang, L. Mahadevan, and J. Aizenberg, "Self-organization of a mesoscale bristle into ordered, hierarchical helical assemblies," *Science* **323**, 237–240 (2009).
- ¹⁴⁷A. W. Feinberg, A. Feigel, S. S. Shevkoplyas, S. Sheehy, G. M. Whitesides, and K. K. Parker, "Muscular thin films for building actuators and powering devices," *Science* **317**, 1366–1370 (2007).
- ¹⁴⁸Y. Zhou, Y. F. Zhang, and C. Q. Chen, "Amplitude-dependent boundary modes in topological mechanical lattices," *J. Mech. Phys. Solids* **153**, 104482 (2021).
- ¹⁴⁹L. L. Geng, W. X. Zhang, X. D. Zhang, and X. M. Zhou, "Topological mode switching in modulated structures with dynamic encircling of an exceptional point," *Proc. R. Soc. London, A* **477**, 20200766 (2021).
- ¹⁵⁰A. Ghatak, M. Brandenbourger, J. van Wezel, and C. Coulais, "Observation of non-Hermitian topology and its bulk-edge correspondence in an active mechanical metamaterial," *Proc. Natl. Acad. Sci. U.S.A.* **117**, 29561–29568 (2020).
- ¹⁵¹L. M. Nash, D. Kleckner, A. Read, V. Vitelli, A. M. Turner, and W. T. M. Irvine, "Topological mechanics of gyroscopic metamaterials," *Proc. Natl. Acad. Sci. U.S.A.* **112**, 14495–14500 (2015).
- ¹⁵²W. Wang, X. L. Wang, and G. C. Ma, "Non-Hermitian morphing of topological modes," *Nature* **608**, 50–55 (2022).
- ¹⁵³P. Baconnier, D. Shohat, C. H. Lopez, C. Coulais, V. Demery, G. During, and O. Dauchot, "Selective and collective actuation in active solids," *Nat. Phys.* **18**, 1234–1239 (2022).
- ¹⁵⁴A. Darabi, X. Xiang Ni, M. Leamy, and A. Alù, "Reconfigurable Floquet elastodynamic topological insulator based on synthetic angular momentum bias," *Sci. Adv.* **6**, eaba8656 (2020).
- ¹⁵⁵Q. Zhang, Y. Chen, K. Zhang, and G. K. Hu, "Programmable elastic valley Hall insulator with tunable interface propagation route," *Extreme Mech. Lett.* **28**, 76–80 (2019).
- ¹⁵⁶C. Zhang, W. K. Cao, L. T. Wu, J. C. Ke, Y. Jing, T. J. Cui, and Q. Cheng, "A reconfigurable active acoustic metalens," *Appl. Phys. Lett.* **118**, 133502 (2021).
- ¹⁵⁷Z. Y. Chen, W. J. Zhou, and C. W. Lim, "Tunable frequency response of topologically protected interface modes for membrane-type metamaterials via voltage control," *J. Sound Vib.* **494**, 115870 (2021).
- ¹⁵⁸W. J. Zhou, Y. P. Su, W. Q. Chen, and C. W. Lim, "Voltage-controlled quantum valley Hall effect in dielectric membrane-type acoustic metamaterials," *Int. J. Mech. Sci.* **172**, 105368 (2020).
- ¹⁵⁹L. H. Wu and X. Hu, "Scheme for achieving a topological photonic crystal by using dielectric material," *Phys. Rev. Lett.* **114**, 223901 (2015).
- ¹⁶⁰W. J. Zhou, B. Wu, Z. Y. Chen, W. Q. Chen, C. W. Lim, and J. N. Reddy, "Actively controllable topological phase transition in homogeneous piezoelectric rod system," *J. Mech. Phys. Solids* **137**, 103824 (2020).
- ¹⁶¹Y. B. Jin, W. X. Zhong, R. C. Cai, X. Y. Zhuang, Y. Pennec, and B. Djafari-Rouhani, "Non-Hermitian skin effect in a phononic beam based on piezoelectric feedback control," *Appl. Phys. Lett.* **121**, 022202 (2022).
- ¹⁶²J. W. You, Q. Ma, Z. H. Lan, Q. Xiao, N. C. Panoiu, and T. J. Cui, "Reprogrammable plasmonic topological insulators with ultrafast control," *Nat. Commun.* **12**, 5468 (2021).
- ¹⁶³Y. F. Wang, Y. Z. Wang, B. Wu, W. Q. Chen, and Y. S. Wang, "Tunable and active phononic crystals and metamaterials," *Appl. Mech. Rev.* **72**, 040801 (2020).
- ¹⁶⁴Y. Ota, K. Takata, T. Ozawa, A. Amo, Z. Jia, B. Kante, M. Notomi, Y. Arakawa, and S. Iwamoto, "Active topological photonics," *Nanophotonics* **9**, 547–567 (2020).
- ¹⁶⁵M. Parto, S. Wittek, H. Hodaei, G. Harari, M. A. Bandres, J. H. Ren, M. C. Rechtsman, M. Segev, D. N. Christodoulides, and M. Khajavikhan, "Edge-mode lasing in 1D topological active arrays," *Phys. Rev. Lett.* **120**, 113901 (2018).
- ¹⁶⁶J. K. Zou, M. K. Yang, and G. Q. Jin, "A five-way directional soft valve with a case study: A starfish like soft robot," in *International Conference on Automation, Control and Robotics Engineering (CACRE)* (IEEE, 2020), pp. 130–134.
- ¹⁶⁷T. Saha, C. Dash, R. Jayabalani, S. Khiste, A. Kulkarni, K. Kurmi, J. Mondal, P. K. Majumder, A. Bardia, H. L. Jang, and S. Sengupta, "Intercellular nanotubes mediate mitochondrial trafficking between cancer and immune cells," *Nat. Nanotechnol.* **17**, 98–106 (2022).
- ¹⁶⁸Y. C. Yao, J. Y. Gao, S. Chen, P. Zhang, L. Sheng, and J. Liu, "LM-jelly liquid metal enabled biomimetic robotic jellyfish," *Soft Rob.* **9**, 1098–1107 (2022).
- ¹⁶⁹M. Garrad, H. Y. Chen, A. T. Conn, H. Hauser, and J. Rossiter, "Liquid metal logic for soft robotics," *IEEE Rob. Autom. Lett.* **6**, 4095–4102 (2021).
- ¹⁷⁰O. Bleu, G. Malpuech, and D. D. Solnyshkov, "Robust quantum valley Hall effect for vortices in an interacting bosonic quantum fluid," *Nat. Commun.* **9**, 3991 (2018).
- ¹⁷¹H. Chen, L. Y. Yao, H. Nassar, and G. L. Huang, "Mechanical quantum Hall effect in time-modulated elastic materials," *Phys. Rev. Appl.* **11**, 044029 (2019).
- ¹⁷²L. Y. Zheng, G. Theocharis, R. Fleury, V. Tournat, and V. Gusev, "Tilted double Dirac cone and anisotropic quantum-spin-Hall topological insulator in mechanical granular graphene," *New J. Phys.* **22**, 103012 (2020).
- ¹⁷³Y. Z. Liu, C. S. Lian, Y. Li, Y. Xu, and W. H. Duan, "Pseudospins and topological effects of phonons in a Kekulé lattice," *Phys. Rev. Lett.* **119**, 255901 (2017).
- ¹⁷⁴M. Serra-Garcia, V. Peri, R. Susstrunk, O. R. Bilal, T. Larsen, L. G. Villanueva, and S. D. Huber, "Observation of a phononic quadrupole topological insulator," *Nature* **555**, 342–345 (2018).
- ¹⁷⁵T. Fukui, Y. Hatsugai, and H. Suzuki, "Chern numbers in discretized Brillouin zone: Efficient method of computing (spin) Hall conductances," *J. Phys. Soc. Jpn.* **74**, 1674–1677 (2005).
- ¹⁷⁶J. Y. Lu, C. Y. Qiu, M. Z. Ke, and Z. Y. Liu, "Valley vortex states in sonic crystals," *Phys. Rev. Lett.* **116**, 093901 (2016).
- ¹⁷⁷D. Xiao, W. Yao, and Q. Niu, "Valley-contrasting physics in graphene: Magnetic moment and topological transport," *Phys. Rev. Lett.* **99**, 236809 (2007).
- ¹⁷⁸R. Zhou, H. Lin, Y. Wu, Jie, Z. F. Li, Z. H. Yu, Y. Liu, and D. H. Xu, "Higher-order valley vortices enabled by synchronized rotation in a photonic crystal," *Photonics Res.* **10**, 1244–1254 (2022).
- ¹⁷⁹X. Ni, "Topological insulating states in photonics and acoustics," Ph.D. dissertation (City University of New York, 2019).
- ¹⁸⁰G. Duclos, R. Adkins, D. Banerjee, M. S. E. Peterson, M. Varghese, I. Kolvin, A. Baskaran, R. A. Pelcovits, T. R. Powers, A. Baskaran, F. Toschi, M. F. Hagan, S. J. Streichan, V. Vitelli, D. A. Beller, and Z. Dogic, "Topological structure and dynamics of three-dimensional active nematics," *Science* **367**, 1120–1124 (2020).
- ¹⁸¹H. Abbaszadeh, M. Fruchart, W. van Saarloos, and V. Vitelli, "Liquid-crystal-based topological photonics," *Proc. Natl. Acad. Sci. U.S.A.* **118**, e2020525118 (2021).
- ¹⁸²S. Shankar, A. Souslov, M. J. Bowick, M. C. Marchetti, and V. Vitelli, "Topological active matter," *Nat. Rev. Phys.* **4**, 380–398 (2022).
- ¹⁸³D. Q. Zhang, Z. Y. Li, and B. Li, "Self-rotation regulates interface evolution in biphasic active matter through taming defect dynamics," *Phys. Rev. E* **105**, 064607 (2022).
- ¹⁸⁴E. Karzbrun, A. Kshirsagar, S. R. Cohen, J. H. Hanna, and O. Reiner, "Human brain organoids on a chip reveal the physics of folding," *Nat. Phys.* **14**, 515–522 (2018).

- ¹⁸⁵Y. Maroudas-Sacks, L. Garion, L. Shani-Zerbib, A. Livshits, E. Braun, and K. Keren, “Topological defects in the nematic order of actin fibres as organization centres of hydra morphogenesis,” *Nat. Phys.* **17**, 251–259 (2021).
- ¹⁸⁶W. A. Benalcazar, B. A. Bernevig, and T. L. Hughes, “Electric multipole moments, topological multipole moment pumping, and chiral hinge states in crystalline insulators,” *Phys. Rev. B* **96**, 245115 (2017).
- ¹⁸⁷X. J. Zhang, L. Liu, M. H. Lu, and Y. F. Chen, “Valley-selective topological corner states in sonic crystals,” *Phys. Rev. Lett.* **126**, 156401 (2021).
- ¹⁸⁸S. Z. Lin, P. C. Chen, L. Y. Guan, Y. Shao, Y. K. Hao, Q. Y. Li, B. Li, D. A. Weitz, and X. Q. Feng, “Universal statistical laws for the velocities of collective migrating cells,” *Adv. Biosyst.* **4**, 2000065 (2020).
- ¹⁸⁹L. Y. Yang, Y. Wang, Y. Meng, Z. X. Zhu, X. Xi, B. Yan, S. X. Lin, J. M. Chen, B. J. Shi, Y. Ge, S. Q. Yuan, H. S. Chen, H. X. Sun, G. G. Liu, Y. H. Yang, and Z. Gao, “Observation of Dirac hierarchy in three-dimensional acoustic topological insulators,” *Phys. Rev. Lett.* **129**, 125502 (2022).
- ¹⁹⁰H. Patel, J. H. Chen, Y. H. Hu, and A. Erturk, “Photo-responsive hydrogel-based re-programmable metamaterials,” *Sci. Rep.* **12**(1), 13033 (2022).
- ¹⁹¹S. H. Zhou, C. H. Bao, B. S. Fan, H. Zhou, Q. X. Gao, H. Y. Zhong, T. Y. Lin, H. Liu, P. Yu, P. Z. Tang, S. Meng, W. H. Duan, and S. Y. Zhou, “Pseudospin-selective Floquet band engineering in black phosphorus,” *Nature* **614**, 75–80 (2023).
- ¹⁹²X. Ni, S. Yves, A. Krasnok, and A. Alu, “Topological metamaterials,” *arXiv:2211.10006* (2022).
- ¹⁹³H. Al Ba’ba’ā, K. Yu, and Q. Wang, “Elastically-supported lattices for tunable mechanical topological insulators,” *Extreme Mech. Lett.* **38**, 100758 (2020).